AUTOMATIC SEGMENTATION OF WALL STRUCTURES FROM CARDIAC IMAGES

A Thesis
Presented to
The Academic Faculty

by

Liangjia Zhu

In Partial Fulfillment
of the Requirements for the Degree
Doctor of Philosophy in the
School of Electrical and Computer Engineering

Georgia Institute of Technology
May 2013

AUTOMATIC SEGMENTATION OF WALL STRUCTURES FROM CARDIAC IMAGES

Approved by:

Professor Patricio Vela,
Committee Chair
School of Electrical and Computer Engineering
Georgia Institute of Technology

Professor Francesco Fedele
School of Electrical and Computer Engineering
Georgia Institute of Technology

Professor Anthony Yezzi, Advisor
School of Electrical and Computer Engineering
Georgia Institute of Technology

Professor Magnus Egerstedt
School of Electrical and Computer Engineering
Georgia Institute of Technology

Professor Allen Tannenbaum, Advisor
School of Electrical and Computer Engineering
Georgia Institute of Technology

Professor Arthur Stillman
Department of Radiology
Emory University

Date Approved: December 6, 2012

献给父亲母亲
献给妻子和儿子
为他们一如既往的关爱和支持

To my parents,

To my wife and my son

for their love and support along my journey of pursuing dreams.

ACKNOWLEDGEMENTS

I would like to thank those who have been supporting me and helping me through my doctorate years.

First, I would like to thank my advisers, Professor Allen Tannenbaum and Professor Anthony Yezzi. From you I have learned not only knowledge and techniques, but how to be a great researcher. It is and will always be my great honor to be a student of you.

I particularly wish to acknowledge my deep gratitude to Professor Tracy Faber who had helped to push my research forward and devoted her life to cardiac imaging analysis, without whom I could not have finished the ventricle segmentation project.

I also would like to thank my thesis committee, Professor Patricio Vela, Professor Francesco Fedele, Professor Magnus Egerstedt, and Professor Arthur Stillman for your helpful comments and suggestions, which have helped to improve my thesis in many aspects.

Thank you to everyone in our great group: Yi Gao, Jehoon Lee, Peter Karasev, Ivan Kolesov, Martin Mueller, Vandana Mohan, Jacob Huang, Ping-Chang Shih, Vikram Appia, and Balaj Ganapathy. Thank you for your help all through the years of my study. And it has always been a pleasure to spend time in the lab, attend group meetings, and share the knowledge and happiness with you.

Thanks to my friends here and in China, for your friendship and support.

To my dear wife Yi Quan, my son Andrew, to my parents and my brother, for everything.

TABLE OF CONTENTS

LIST OF TABLES

LIST OF FIGURES

SUMMARY

Medical image analysis is a multidisciplinary research field that has direct impact on the diagnosis, treatment, intervention, and prognosis of diseases. One important topic in this field is segmenting wall structures from different cardiac medical imaging modalities such as computed tomography (CT) and magnetic resonance imaging (MRI). This task is typically done by radiologists either manually or semi-automatically, which is a very time-consuming process. To reduce the laborious human efforts, automatic methods have become popular, especially as the size of medical imaging data becomes larger and larger with the development of image acquisition techniques. A common solution to the automatic segmentation problem is fitting the model of a wall structure to match image content. However, several issues need to be addressed while applying the model for segmentation, *e.g.*, how to train a model and how to initialize it in an image, when taking the wide variability of image data into account. In this thesis, features insensitive to data variations are explored to segment the ventricles from CT images and extract the left atrium from MR images. As applications, the segmentation results are used to facilitate cardiac disease analysis. Specifically,

1. An automatic method is proposed to extract the ventricles from CT images by integrating surface decomposition with contour evolution techniques. In particular, the ventricles are first identified on a surface extracted from patient-specific image data. Then, the contour evolution is employed to refine the identified ventricles. The proposed method is robust to variations of ventricle shapes, volume coverages, and image quality.

2. A variational region-growing method is proposed to segment the left atrium

from MR images. Because of the localized property of this formulation, the proposed method is insensitive to data variabilities that are hard to handle by globalized methods.

3. In applications, a geometrical computational framework is proposed to estimate the myocardial mass at risk caused by stenoses. In addition, the segmentation of the left atrium is used to identify scars for MR images of post-ablation.

CHAPTER I

INTRODUCTION

Cardiovascular diseases are the leading causes of non-accidental death in the world [77]. The prognosis or diagnosis of these diseases commonly rely on quantitative study of anatomical wall structures such as the ventricles and left atrium from cardiac images. Automatic delineation of those structures that is robust to data variations is an active research field. A common strategy used in the literature combines global localization with local refinement sequentially. To this end, a model of the structure to be segmented is built and used to guide the segmentation process. The introduction of high level models can to some extent handle challenges such as poor boundaries, varying structure shapes, and difference of volume coverages that methods driven by image data face. However, building a generic model with high adaptivity to data variations is not a trivial task. In this thesis, the segmentation problem is formulated from another perspective that explores features from image data on-line and captures the global structure. In particular, this thesis presents automatic methods to segment the ventricles from CT images and extract the left atrium from MR images. In applications, a computational method is proposed for estimating the myocardial mass at risk caused by stenoses, given the segmentation of ventricles. In addition, given the segmentation of the left atrium, an effective way is presented to identify scar tissue for atrial fibrillation analysis. Specifically,

In Chapter 2, the problem of segmenting ventricles from CT images is addressed. In the proposed method, the ventricles are extracted sequentially by first searching for the left ventricle (LV) on the blood pool surface. To this end, the geometric features that distinguish the LV from the other structures on the surface are utilized. Then,

the location of the LV is used to infer the location of the right ventricle (RV). Finally, these rough localization results are refined by using contour evolution techniques. In this formulation, all computations are based on the information obtained from images to be segmented, rather than on training images. Therefore, the method is robust to data variations.

In Chapter 3, a more challenging problem is investigated: extracting the left atrium (LA) from MR images in presence of poor boundaries and thin layer of the LA wall. The same idea as in segmenting the ventricles is used, *i.e.*, exploring features that are robust to data variabilities. To do so, the problem is formulated as a problem in variational region growing. In particular, the method begins by searching for a seed region of the LA. Then, a growing process starts to capture the LA by incorporating the robust statistics of image intensities and a shape constraint coming from a LA shape prior. The Zernike moments are used for representing the shape prior, which are invariant to rotation, translation, and scaling. Thus, this formulation separates segmentation from registration, *i.e.*, removing the requirement of estimating pose parameters while applying the shape prior.

Two applications of wall structure segmentation in cardiac disease analysis are summarized in Chapter 4. In the first application, it elaborates on how to compute the myocardial mass at risk caused by stenoses given the segmentation of the LV. The computation is performed on the LV surface to cluster surface points according to their nearest distances to coronary arteries. The proposed computational framework removes the requirement of registering images from different modalities since all components are extracted from CT images. In the second application, the scar tissue resulted from post-ablation in an atrial fibrillation treatment is identified. A thin wall is generated from the segmented LA, which is used as a region of interest (ROI) for searching the scar tissue. Then, the intensities inside the ROI is represented by a Gaussian mixture model, and the component with a higher mean intensity implies

the scar region.

The rest of this chapter will review some of the related work from the literature.

1.1 Ventricles Segmentation

Prognosis and diagnosis of cardiovascular diseases frequently requires quantitative evaluations of the ventricle volume, mass, and ejection fraction. The delineation of the ventricles is involved in all of these evaluations, which is a challenging task because of factors such as shape variability between different cardiac cycles and between different patients, weak edges between epicardium and heart fat or soft tissues.

To get an accurate segmentation, model-based methods have become dominant in this research [76]. Typically, a heart model is built by learning the geometric or intensity features of the heart from cardiac images. While in segmentation, a commonly used framework is first globally aligning the model to an image and then deforming this model to fit image content. Global localization is achieved by detecting the geometric or intensity features of the heart. Local deformations are performed by optimizing an objective function defined between the model parameters and image features. In particular, the model-based methods can be roughly categorized based on whether these models are applied explicitly or implicitly for segmentation. In the first type of methods, models created off-line are fitted to images for segmentation. For example, in active shape models (ASMs) [17, 30], a statistical shape model called the Point Distribution Model is learned from a set of aligned shapes by using the principal component analysis (PCA) technique, which is iteratively aligned to image boundaries. Active appearance models (AAMs) extend this idea by incorporating gray level information [16] and were used in segmenting the left and right ventricles from MR images [61]. The deformations allowed in the parametric models such as ASMs and AAMs are restricted to the shape space where the heart models are embedded. The shape space may be represented by 3D diffusion wavelets [26], which encode

shape variations hierarchically. A more flexible way of incorporating shape priors is by using deformable models that are capable of adapting to local image content. For example, Ecabert *et al.* [25] modeled the whole heart as a multi-compartment, triangulated surface obtained from training images. The local adaptation was achieved by progressively optimizing the piecewise affine transformations of this model to match image boundaries. In [89], a mean shape was aligned to an image by estimating similarity transformations, which was then deformed to fit the heart boundaries with the help of landmark points on the interventricular septum. Instead of deforming a pre-aligned model, multi-atlas-based methods use shape information implicitly by directly registering each atlas image to a target image. Then, the labels of all atlases are combined to form a consistent solution. Model-free methods have also been widely used to explore the characteristics of heart geometry or intensity distribution from other perspectives. For example, a random forest method was utilized to learn the geometric and intensity features for delineating the myocardium [54]. For a comprehensive literature review of heart segmentation, see [76, 67] and references therein.

Active contour models have been widely used in medical image segmentation because of their flexibility and robustness. In these models, energy functionals are commonly defined over image features such as edges [13], region statistics [14], and a combination of edges and regions [51, 52], which are optimized by using gradient descent techniques. Prior information can be incorporated as well to guide the optimization process. For example, an active contour model was evolved in the shape space of the LV obtained by applying the PCA to manually segmented images [78]. To account for local deformations, pixel-wise stochastic level sets was used to represent a shape prior for extracting the endocardium [65]. A shape constraint defined between two consecutive image slices was employed to control the search space of myocardial contours [40]. Coupled active contours have been proposed with distance constraints

between contours for myocardium extraction[58], cortex segmentation [85], and cell tracking [96].

One important but less studied topic is how to localize the heart region initially, especially for these methods using deformable models, which tend to get stuck in undesirable local extrema when started without a good initialization. Typically, the geometric features of the heart are used for localization. In [40], the blood pool of the heart was extracted via thresholding. After that, the connected component that is most circular and convex but least eccentric was selected as the endocardium and approximated by a circle. Then, this circle was expanded to generate the epicardium. Similar empirical rules were used in identifying the LV cavity [57]. To capture a more generic heart shape, the generalized Hough transform was utilized for heart detection [25]. In [89], localization was achieved by searching for a similarity transformation in a hierarchical way: starting from translation mainly to translation-orientation and then to a full similarity transformation estimation. Different image features were used at different stages of the transformation estimation. Atlas-based registration has also been used for coarse initialization [26].

One fact that has been ignored in the literature for the localization is that the LV is a salient component on the heart surface. This is where the shape decomposition/segmentation technique can be utilized to cluster the surface into *meaningful* components based on some given criteria as in computer graphics and geometric modeling [73, 3]. For example, a surface may be hierarchically decomposed into regions of deep concavities by using fuzzy clustering and graph partition techniques [46]. Prominent feature points [45] have also been used to cluster a surface into meaningful regions. Applications of shape segmentation in medical imaging can be found in heart modeling from images [5] and aneurysm neck detection on vessel surfaces [11]. Active contour models have been applied on surfaces to refine coarse segmentations [41] or

extract objects of interest [50]. Among the few applications of the shape decomposition techniques to cardiac image segmentation, the *narrowing* of vessels around the LA was detected by merging local features based on given criteria to extract the LA [38]. As for the LV localization, the region near the LV is even much more recognizable from the heart surface than from the volumetric data, which can be identified by a deep concave contour.

1.2 Left Atrium Segmentation

Automatic segmentation of the LA from MRI data is a challenging but major task in medical imaging analysis. An important application is concerned with the treatment of left atrial fibrillation [60]. Atrial fibrillation is a cardiac arrhythmia characterized by unsynchronized electrical activity in the atrial chambers of the heart. The catheter ablation, as one of the treatments for such arrhythmia, uses an intra-cardiac catheter to target specific parts of the LA for radio-frequency ablation [37]. Application of radio-frequency energy to the cardiac tissue causes thermal injury, which in turn results into scar tissue. Successful ablation can eliminate, or isolate, the problematic sources of electrical activity and effectively cure atrial fibrillation. In order to perform such ablation, the extraction of the LA from the late gadolinium enhancement MR (LGE-MR) images is required and is often performed manually, which is a very time-consuming task. However, automatic segmentation of the LA is challenging due to the following factors: 1) the LA size is relatively small as compared to the left ventricle (LV) or lungs in cardiac MR images; 2) boundaries are not clearly defined when the blood pool goes into the pulmonary veins from the LA; 3) the shape variability of the LA is large across subjects.

In the literature, heart segmentation has been investigated for decades, of which the main focus has been on extracting the ventricles [76, 67]. Advances have been made in whole heart segmentation from CT and MR images [89, 25, 79, 95]. Heart

models are used in many of the state-of-the-art methods for segmentation. In general, the anatomical structure of heart is modeled either by a triangulated surface or a labeled image. A cost functional is commonly defined driven by the model parameters and image content. Once the model is globally localized, the cost function is optimized by deforming the model to match image information. These methods achieve high overall accuracy since the whole heart is modeled so that the components with strong features, *e.g.* the LV, help to reduce possible mis-alignments.

However, there has not been as much work reported for the automatic segmentation of the LA from MR images. Some nice research aimed at LA segmentation was focused on MR Angiography (MRA) data [39, 42, 22], where the LA blood pool is highlighted. The geometric characteristics of the heart chambers have been used [39, 42] to identify the LA on the blood pool surface using a divide-and-merge strategy. In particular, the surface is decomposed into different subdivisions based on the observation that neighboring heart chambers can be separated by cutting the locations where the blood pool narrows. The challenges these surface-decomposition-based techniques face include the wide variability of intensity distributions and of the anatomic structures of the LA across subjects. To capture a patient specific LA from C-Arm CT images, the LA chamber and pulmonary veins are modeled separately as parts of a LA model [90].

In contrast to surface-based modeling, atlas-based methods consider the LA segmentation from another perspective by using transformations found after registering training images to a target image to align the labels of the training images for segmentation. Different strategies, e.g., weighted voting [22], are used to build a consistent solution for the final segmentation. The initial registered atlases can also be refined by using a region-based active contour model [52]. Another common way of representing an anatomical surface is by learning a subspace of the shapes using the principal component analysis (PCA) technique. In [31], the shape space of the LA was defined

as a linear combination of eigen-shapes returned by applying PCA to training label images. Then, segmentation was accomplished via evolving active contours in the shape space.

One common feature shared with most of the methods described so far is that they start with some global localization and then capture local details. This strategy works well when global features of a given object are well-defined, but may not hold for small structures such as the LA in an MR image, since the contribution to a cost functional may be overwhelmed by large structures such as the LV or strong artifacts associated with image quality. Instead of starting globally, region growing provides another perspective to the problem that begins locally to capture the entire target. This local property makes it more adaptive to variations of the dataset. In region-growing approaches [97], starting from seed regions, voxels neighboring to a given voxel are merged according to an aggregation criterion. Image intensity homogeneity is a widely used criterion in a growing process. For example, the statistics of intensities in a region are used to evaluate the homogeneity for region growing [94, 33]. Shape priors can be naturally incorporated into a growing process to segment complex objects. Typically, these priors are defined as some distance between reference and observed shapes. A point-wise metric such as the signed distance function between two shapes may be utilized with the prior information [55, 69]. To this end, the reference shape needs to be aligned to the observed shape before computing the shape distance. A more abstract way of defining shape distance employs shape moments, which removes the requirement of aligning shapes for the distance computation. Legendre moments has been proposed to represent a shape prior for 2D images [28]. The results in [47] demonstrate the advantages of using the Zernike moments in 2D image recognition over other moments-based priors in terms of accuracy and robustness. The generalization to the 3D case was reported in [62].

1.3 Estimation of Myocardial Mass at Risk

Prognosis and treatment of cardiac-vascular diseases frequently require the determination of the myocardial mass at risk caused by coronary stenoses. A previous study [71] shows that the regional myocardial mass at risk depends on the shape and content of the myocardium distal to coronary artery occlusions. This has been commonly used to estimate the myocardial area at risk. In one work [27], a 3D model of the coronary artery tree was aligned to the LV epicardial surface built from perfusion SPECT images to estimate the anatomic area at risk. Then, the mass estimation was simplified by assuming a uniform thickness for the myocardium. In another work [53], each tissue voxel was assigned to its nearest arterial branch to determine the dependent myocardial region using micro-CT images.

Essentially, the mass estimation can be formulated as a clustering problem, which associates points on the LV surface with coronary arteries based on the shortest distance criterion. For example, Dijkstra's algorithm [24] was used to associate a region with its closest coronary on the LV epicardial surface to compute the coronary perfusion territories from CTA [7]. In fact, Dijkstra's algorithm has been widely used for reconstructing a distance field on a triangulated surface. Staring from a source point, it iteratively updates the distance information by expanding with the highest priority for the point of the minimal distance to the source point. Because of the *discretized* property that the distance is only evaluated through triangle edges, its accuracy is affected by surface resolution. In a continuous domain, the distance field can be reconstructed by solving the Eikonal equation [72]. The fast marching method [72, 49] solves the equation by exploring points in a Dijkstra-like manner. The improvement is made when updating the distance information, where the update is determined by solving a quadratic equation on a surface triangle. The fast sweeping method [88, 83] solves the Eikonal equation by decomposing the directions of characteristics of the equation into a finite number of groups such that each sweeping ordering can

simultaneously follow the causality of a group of characteristics in certain directions. In this way, two sweeps are enough to reconstruct the distance values for 1D case. These two solvers provide approximations to the solution of the Eikonal equation. To reconstruct distance field with high order accuracy, exact geodesics can be computed on a triangulated surface by propagating distance information like tracing rays emanating from a source point via virtually *unfolding* triangles [75, 9].

1.4 Segmentation of Scar Tissue from MR Images

The delay-enhanced MRI (DE-MRI) technique provides an effective way of imaging scarring and fibrosis tissue of atria. Segmentation of the LA from DE-MRI images can be used in atrial fibrillation (AF) treatment to select suitable candidates for ablation therapy and subsequent monitoring of the therapy. Challenges arise in this task due to the thin thickness of the LA myocardium, low resolution of imaging and signal-to-noise ratio. This is an open problem as shown by the holding of a workshop at ISBI-2012 [35].

In the literature, the scar tissue is mainly determined manually [60, 36], which is very time consuming and prone to observer variability. To achieve automatic segmentation, one observation widely used is that the scar tissue resides around the LA wall and has higher intensity values than its surrounding tissues. In [66], K-means clustering was used to classify voxels inside the manually segmented LA wall as scar or non-scar class. The same idea was used in [84], which models the intensity values inside the LA wall as a mixture of Gaussians and the component with a higher mean value is selected as the scar tissue. The classification problem has also been formulated as Markov random fields and solved by using graph-cuts technique [43].

CHAPTER II

SEGMENTATION OF VENTRICLES FROM CT IMAGES

In this Chapter, an automatic method is presented to segment the left and right ventricles from CT images. In this method, the LV and RV are extracted sequentially by combining global localization with local deformations. The key observation in this work is that the ventricles are distinctive components on the heart surface, which can be separated from other structures by using shape decomposition techniques. Once the ventricles are localized in the image, the contour evolution technique is utilized to refine the segmentations.

2.1 Preliminaries

In this section, some basics are briefly reviewed especially the active contour models and distance computation on surfaces, which are to be used through the proposed method.

2.1.1 Active Contour Models

Since the introduction of active contour models by Kass *et al.* [44], contour evolution techniques have been widely used in image segmentation. The basic idea behind these models is to deform a closed contour such that an energy functional defined over the contour is minimized. In general, the energy functional is defined over image features of edges [13], regions enclosed by contours [14], or a combination of edges and regions [51, 52]. Osher and Sethian [63] proposed a numerical solution to the minimization problem involved in the active contour models. In this formulation, the contour is embedded as the zero level set of a function with one additional dimension. This framework has become popular because of its advantage in handling topological

changes during the contour evolution process over the traditional parametric active contour models. In this work, active contour models are utilized to integrate image features from edges, regions, and statistics. This section offers a brief summary of these three types of energy functionals to be used, which follows the formulation in [87] for these models.

Let C be a closed contour and $\phi : \Omega \to \mathbb{R}$ a level set function such that $\phi > 0$ represents the inside of C and $\phi < 0$ outside, where Ω is an open region indicating the image domain. Typically, ϕ is a signed distance function. The contour C can be represented as

$$C = \{x \mid \phi(x) = 0,\ x \in \Omega\}. \tag{1}$$

Geometric measurements are related to ϕ, *e.g.*,

$$\begin{aligned} Length\{\phi = 0\} &= \int_\Omega \delta(\phi(x))|\nabla\phi(x)|dx \\ Area\{\phi > 0\} &= \int_\Omega H(x)dx \end{aligned}, \tag{2}$$

where $H(x)$ is the Heaviside function

$$H(x) = \begin{cases} 1 & \text{if } x \geq 0 \\ 0 & \text{if } x < 0 \end{cases}, \tag{3}$$

and $\delta(x)$ is the Dirac delta function

$$\delta(x) = \frac{d}{dx}H(x). \tag{4}$$

The geometric active contour model [13] can be formulated as follows:

$$E(\phi) = \int_\Omega g(x)\delta(\phi(x))|\nabla\phi(x)|dx, \tag{5}$$

where $g : \Omega \to \mathbb{R}^+$ is a positive function that encodes the edge information of an image. This energy measures a weighted length of the contour C over the image feature g, the minimization of which gives the geodesics or the minimal length contour defined

by the image content. The first variation of $E(\phi)$ with respect to ϕ is

$$\begin{aligned}\frac{\partial E(\phi)}{\partial \phi} &= -|\nabla\phi|\nabla\cdot\left(g(x)\frac{\nabla\phi}{|\nabla\phi|}\right) \\ &= -g(x)|\nabla\phi|\kappa - \nabla g(x)\cdot\nabla\phi\end{aligned}, \tag{6}$$

where κ is the curvature of the contour at x. Thus, the minimization of Equation (5) can be obtained by using the gradient descent method as

$$\begin{cases}\dfrac{\partial\phi}{\partial t} = g(x)|\nabla\phi|\kappa + \nabla g(x)\cdot\nabla\phi \\ \dfrac{\partial\phi}{\partial\overrightarrow{n}}\Big|_{\partial\Omega} = 0 \\ \phi(0) = \phi(C_0)\end{cases}, \tag{7}$$

where $\partial\Omega$ is the boundary of Ω and t is an artificial time that tracks the evolution of the contour C. The first term in the gradient descent flow shrinks the contour in the most efficient way based on contour curvatures, and the second term attracts the contour to real boundaries.

Similarly, a region-based functional or Chan-Vese energy [14] is defined as

$$E(\phi, c_1, c_2) = \int_\Omega \Big(I(x) - c_1\Big)^2 H(\phi(x))dx + \lambda\int_\Omega \Big(I(x) - c_2\Big)^2(1 - H(\phi(x)))dx, \tag{8}$$

where c_1 and c_2 are the intensity means inside and outside of the contour C, respectively,

$$c_1 = \frac{\int_\Omega H(\phi(x))I(x)dx}{\int_\Omega H(\phi(x))dx}, \tag{9}$$

$$c_2 = \frac{\int_\Omega (1 - H(\phi(x)))I(x)dx}{\int_\Omega (1 - H(\phi(x)))dx}. \tag{10}$$

Typically, λ is set to $\lambda = 1$. The gradient descent flow of the Chan-Vese energy is

$$\begin{cases}\dfrac{\partial\phi}{\partial t} = -(I(x) - c_1)^2 + (I(x) - c_2)^2 \\ \dfrac{\partial\phi}{\partial\overrightarrow{n}}\Big|_{\partial\Omega} = 0 \\ \phi(0) = \phi(C_0)\end{cases}. \tag{11}$$

Note that regularization terms were used in the original Chan-Vese energy functional [14] to constrain the evolution process.

The last active contour model to be reviewed is a variational region-growing method [33] that utilizes the statistics of image intensities to drive the contour evolution process. To compute the statistics, a feature vector is defined at each pixel $x \in \Omega$ of an image I as

$$\boldsymbol{f}(x) = (MED(x), IQR(x), MAD(x))^T \in \mathbb{R}^3, \tag{12}$$

where $MED(x)$, $IQR(x)$, and $MAD(x)$ are the intensity median, inter-quartile range, and median absolute deviation around a neighborhood of x, respectively. Let $G : \Omega \to \mathbb{N} \cup \{0\}$ be an indication function, where 0 indicates background and a positive integer indicates seed regions inside an object. Then, these seed regions are characterized by the probability density function of the feature vectors as

$$p(\boldsymbol{f}) = \frac{1}{|G|} \sum_{x \in G} K_\eta(\boldsymbol{f} - \boldsymbol{f}(\boldsymbol{x})), \tag{13}$$

where K is a kernel function. The region-growing energy functional [33] is defined as

$$E(\phi) = \lambda \int_\Omega -p(\boldsymbol{f}(x))H(\phi(x))dx + (1-\lambda) \int_\Omega \delta(x)|\nabla\phi(x)|dx, \tag{14}$$

where the first term measures the intensity homogeneity inside a contour where $\phi > 0$, and the second term is the length of the contour, which controls the smoothness of the final result. The gradient descent flow of $E(\phi)$ is

$$\frac{\partial\phi}{\partial t} = \lambda\delta(\phi(x))p(\boldsymbol{f}(x)) + (1-\lambda)|\nabla\phi(x)|\nabla \cdot \Big(\frac{\nabla\phi(x)}{|\nabla\phi(x)|}\Big). \tag{15}$$

2.1.2 Distance Computation on Surfaces

The distance field starting from given points on a surface M can be reconstructed by solving the Eikonal equation [72]

$$|\nabla T| = F(x), \tag{16}$$

where T is called the arrival time. Physically, the solution of this equation gives the shortest time needed to travel from the starting points to any point $x \in M$ with $F(x)$ being the time cost at x. The numerical solution of this equation on a triangulated surface can be found by using the fast marching algorithm [49]. In this algorithm, the distance information from the starting points is propagated in all directions by approximating the gradient term in Equation (16) in a upwind fashion through ordering points to be updated in a special way. The main steps of the fast marching method are summarized as follows:

Initialization

Label the given points as *Alive* and set $T = 0$. Mark all neighbors of *Alive* as *Close* and all other points as *Far*.

Loop

1. Change the status of the point with the smallest T value to *Trial*.
2. Move the *Trial* point to *Alive* list.
3. Move all neighbors of *Trial* to *Close* list if they are not *Alive*; If a neighbor is in the *Far* list, move it to *Close* list.
4. Update the values of T for all the neighbors using the points that are *Alive*.
5. Repeat the process until the *Close* list is empty or the value of T is greater than a threshold.

This process actually expands points in the same way as the Dijkstra's algorithm [24] does, but it gives a continuous solution as compared to the original Dijkstra's algorithm. The key step is computing the value of T. Suppose the surface M can be represented by a triangle mesh. The numerical algorithm proposed in [49] breaks down the updating step into two cases, *i.e.*, non-obtuse and obtuse triangles, so that

the values of T are updated in a upwind fashion. Specifically, if the triangle to be updated is non-obtuse as shown in Figure 1(a), then the updating steps are as follows:

1. Solve the trigonometry on the triangle ABC for t:

$$(a^2 + b^2 - 2ab\cos\theta)t^2 + 2bu(a\cos\theta - b)t + b^2(u^2 - F^2a^2\sin^2\theta) = 0, \qquad (17)$$

   where $u = T(B) - T(A)$, t is the potential increment for $T(C)$.

2. If $u < t$ and $a\cos\theta < \overline{CD} < \dfrac{a}{a\cos\theta}$,
   then $T(C) = \min\{T(C), T(A) + t\}$;
   else $T(C) = \min\{T(C), T(A) + bF, T(B) + aF\}$.

For the obtuse case, suppose the obtuse angle is at vertex C as shown in Figure 1(b). The triangle to be updated is recursively unfolded until a new vertex B is included in the extended region. Then the vertices are connected by a virtual edge from B to C, which splits the original triangle into two acute ones (see [49] for details). After that, the value of C can be updated by using the scheme for non-obtuse triangle.

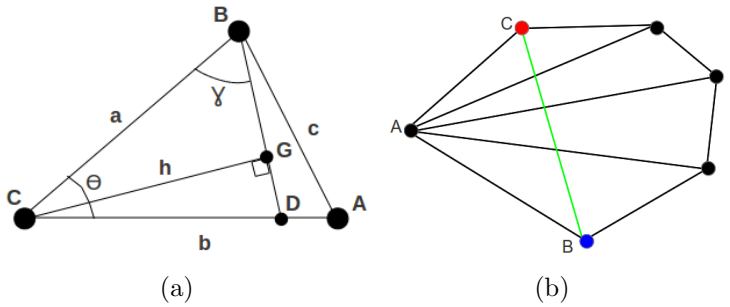

(a) (b)

Figure 1: Trigonometry of a triangle ABC for updating $T(C)$ when angle C is (a) acute and (b) obtuse.

2.2 Proposed Method

The flowchart of the proposed method is shown in Figure 2. The overall segmentation process consists of ventricles localization and myocardial wall extraction. First, the LV is localized by using the shape segmentation technique. Then, the RV is identified on a

heart surface constructed based on the segmentation of the LV. Finally, the myocardial wall, lying between the epicardial and endocardial surfaces of the ventricles, is refined by employing an active contour model with a constraint based on the localization results. The main steps are described in the following sections.

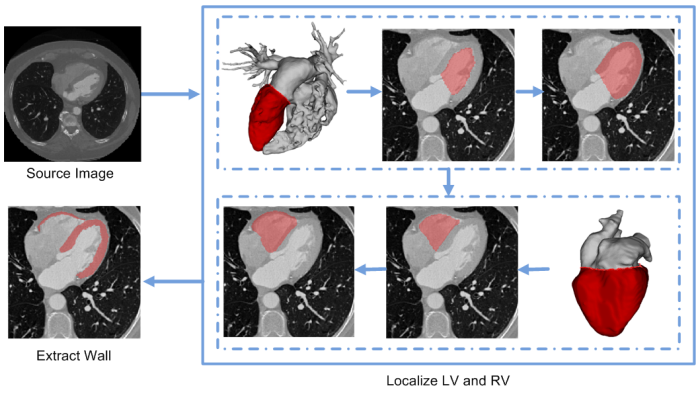

Figure 2: Flowchart for segmenting the ventricles from CT images.

2.2.1 Left Ventricle Localization

Assume that the orientation of a CT image is given and intensity contrast exists between blood pool and the myocardium. The localization of the LV is determined via searching for a deep concave boundary on the blood pool surface as follows:

2.2.1.1 Extract Blood Pool Surface

The extraction of the blood pool surface is carried out by a few mature techniques in the computer vision and graphics: Since CT images have calibrated gray levels, the source image is thresholded to highlight the blood pool region. Then, a morphological opening operator is applied to remove noisy arteries and cut spines that may be residing in the same connected component of the heart. The largest connected component is chosen as a mask for the blood pool. The marching cube method [56] is used to triangulate the blood pool mask. Again, only the largest connected surface is taken as the blood pool surface.

2.2.1.2 Detect Apex Point

Suppose the coordinate system of a source image is Left-Posterior-Inferior (LPI) as shown in Figure 3. In this system, XYZ coordinates trace from left to right, posterior to anterior, and inferior to superior. Even though the long axis of pig and human hearts has different orientations [18], the directions of *left* and *right* are clearly defined from the inferior view. The apex point is a salient feature that can be used to locate the LV as follows: 1) estimate the orientation of ventricles; 2) search for the LV apex, which is the *left* tip point with respect to the estimated orientation.

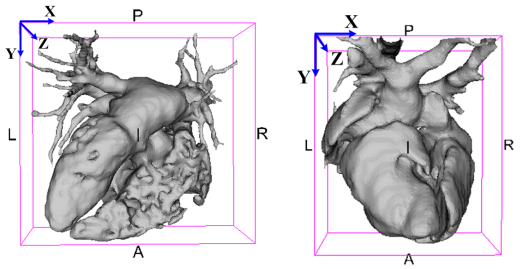

(a) (b)

Figure 3: Orientation of (a) human and (b) pig blood pool surfaces in the source image coordinate system. The reference directions are left(L), right(R), posterior(P), anterior(A), inferior(I), and superior(S).

To estimate the orientation of ventricles, the convex hull of the blood pool surface M_{bp} is first constructed. Let $K(\tilde{p})$ be the Gaussian curvature at vertex $\tilde{p}$ of the convex hull. The vertices used to estimate ventricle orientation are

$$V_{ch}(\tilde{p}) = \{\tilde{p} | K(\tilde{p}) > \mu_K + \sigma_K \cap y(\tilde{p}) > t_y\}, \tag{18}$$

where μ_K and σ_K are the mean and standard deviation of $\{K(\tilde{p})\}$, and a threshold t_y determines the region of interest, which is empirically set as $t_y = y_{min} + 0.5(y_{max} - y_{min})$, to select points in the bottom half of the source image in the posterior-anterior or Y direction. Then, all points $\tilde{p} \in V_{ch}$ are translated as $\tilde{p}_s = \tilde{p} - \mu_{bp}$, where μ_{bp} is the centroid of M_{bp}. The PCA technique is used to find the principal component of these translated points $\tilde{p}_s$ as the orientation of the ventricles, denoted by $\mathbf{H}$. The

positive direction is chosen so that $\mathbf{H}$ has negative component in the Y direction. A plane L_O passing through μ_{bp} with normal $\mathbf{N} = \mathbf{Z} \times \mathbf{H}$ defines a reference plane such that the LV points are mainly above the plane and otherwise for the RV.

Let $\lambda_{max} \in \mathbb{R} \quad s.t. \quad \lambda_{\max} = \max(\tilde{p}_s \cdot \mathbf{H})$. A reference point is defined as $p_{rf} = \mu_{bp} + \lambda_{max}\mathbf{H}$. A constraint region-labeling process is employed to search for a neighborhood of the LV apex as follows: First, the corresponding points of V_{ch} on the surface M_{bp} are sorted in an ascending order based on their distances to p_{rf}, denoted by $\{p_j\}$, $j = 1 \cdots n_{ch}$, where n_{ch} is the cardinality of the set V_{ch}. Then, the distance field starting from p_1 is reconstructed by using the fast marching method [49]. All points with their distances smaller than a threshold t_n is labeled as 1. After that, the unlabeled points with smallest index in $\{p_j\}$ is checked. If its distance to p_{rf} is smaller than the maximum distance between the labeled points and p_{rf}, then this point is selected to start the labeling process again and the points within the range of t_n are labeled as 2. Let μ_1 and μ_2 be the centroids of these two labeled regions, respectively. The region with a larger projection $(\mu_i - \mu_{bp}) \cdot \mathbf{N}$, $i = 1, 2$, is selected as a neighborhood around the LV apex, denoted by N_{apx}. As a special case when only one labeled region is found, this region is automatically selected as N_{apx}. Finally, the point in N_{apx} with the largest projection in $\mathbf{H}$ direction is chosen as the apex point, denoted by p_{apx}. Typically, the threshold t_n is set as $t_n = 30$ mm.

An illustration of the apex detection process is shown in Figure 4. In this figure, two neighborhoods are identified around the LV and RV apexes, respectively. Given the constructed plane L_O, the LV apex is correctly labeled both on the human and pig blood pool surfaces.

2.2.1.3 Find an Initial Cut Contour

The initial cut contour, denoted by C_0, is determined based on the distance field starting from p_{apx}. Similar as in Section 2.2.1.2, the distance field is computed by

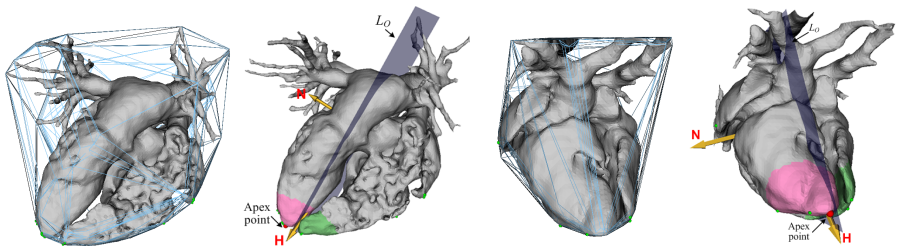

(a) (b) (c) (d)

Figure 4: Apex detection for human and pig hearts. Convex hull with high curvature points (green) for the human (a) and pig (c) hearts. Neighborhoods around the apex points of human (b) and pig (d) hearts. The detected apex points are marked with red dots.The vector **H** represents the orientation of the ventricles. The plane L_O with normal **N** identifies the directions of *left* and *right*.

using the fast marching method [49]. The isocontours/level-sets of this distance field is obtained by sampling this field evenly at an interval of 2 mm (see Figure 5(a)). The length of an isocontour increases gradually and then drops slightly while tracing the distance field along the LV. After that, it goes up first and then drops rapidly as the distance is propagating to the RV and the other regions, which behaves like a Gaussian function (see Figure 5(b)). Thus, the changes of isocontour lengths along the distance field can be modeled as a bi-modal function to capture the different paces of these changes. Specifically, suppose the total length of an isocontour at distance d can be modeled by

$$h(d, \tilde{d}) = \begin{cases} c_0 + c_1 d + c_2 d^2 & \text{if } d \leq \tilde{d} \\ a e^{-\frac{(d-\mu)^2}{2\sigma^2}} & \text{if } d > \tilde{d} \end{cases}, \tag{19}$$

where $\tilde{d}$ is serving as a turning point for these two modes. Let (d_i, l_i), $i = 1 \cdots n$, be a pair of a sampled distance and its corresponding isocontour length, where n is the number of samples over the distance field. Then, choose the isocontour at d_{j^*} as the initial cut contour, where j^* is determined by searching for the optimal turning point

that minimizes the least-squares fitting error,

$$j^* = \arg\min_{j} \Big(\arg\min_{c_0,c_1,c_2} \sum_{i=1}^{j} \left(h(d_i, d_j) - l_i\right)^2 + \arg\min_{a,\mu,\sigma} \sum_{i=j+1}^{n} \left(\log h(d_i, d_j) - \log l_i\right)^2 \Big) \tag{20}$$

Here, d_j is a sample point serving as a trial turning point. The optimal turning point d_{j^*} is obtained by exhausting all elements in $\{d_j\}$, $j = 1 \cdots n$. An illustration of the model fitting process described above is shown in Figure 5.

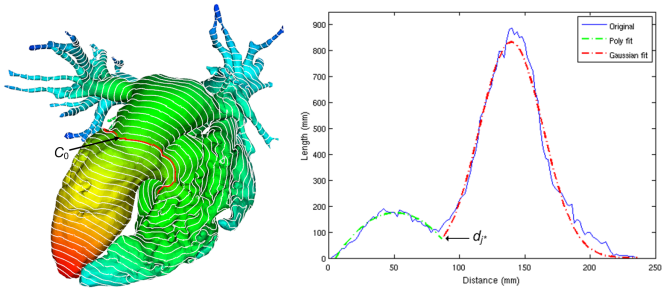

(a) (b)

Figure 5: Detection of the initial cut contour. (a) Distance field from the apex with isocontours (measured in mm). The initial cut contour C_0 is marked in red. (b) The length of isocontours vs. distance, and the determination of the optimal turning point d_j^*.

2.2.1.4 Refine the Cut Contour

The geometric active contour model [48, 13] is used to refine the initial cut contour C_0. Suppose a contour on the surface M_{bp} can be represented by the zero level set of a function $U : M_{bp} \to \mathbb{R}$ with $U(C(p,t)) = 0$, where $C(p,t)$ is a family of contours on M_{bp}. Let $g : M_{bp} \to \mathbb{R}^+$ be a positive function that attracts an active contour to a conceptually desired boundary [41],

$$g(p) = \frac{1}{1 + \Big(|\kappa(p)|/S\Big)^2}, \tag{21}$$

where $\kappa(p)$ is the mean curvature at p, and S is a constant for scales that was empirically set as $S = 0.01$. As in [41], κ is set to zero if it is positive. The geometric

active contour model on the surface M_{bp} is defined as

$$E(U) = \int_{M_{bp}} g(p)\delta(U(p))|\nabla_{M_{bp}} U(p)|dp, \tag{22}$$

where $\delta(U)$ is the Dirac delta function. The energy $E(U)$ evaluates a weighted contour length. Similar as in $\mathbb{R}^n$, the gradient descent flow of $E(U)$ is

$$\begin{cases} \dfrac{\partial U}{\partial t} = |\nabla_{M_{bp}} U|\nabla_{M_{bp}} \cdot \left(g(p)\dfrac{\nabla_{M_{bp}} U}{|\nabla_{M_{bp}} U|} \right) \\ \dfrac{\partial U}{\partial \overrightarrow{n}}|_{\partial M_{bp}} = 0 \\ U(0) = U(C_0) \end{cases}, \tag{23}$$

where ∂M_{bp} is the boundary of M_{bp} and $\overrightarrow{n}$ is the intrinsic outward normal of ∂M_{bp}. Here, $\nabla_{M_{bp}}$ is the del operator on M_{bp}. This flow drives a contour to a desired boundary while minimizing the weighted contour length. In particular, it moves a contour on M_{bp} by its geodesic curvature when $g = 1$, which produces the contour of the shortest length.

Numerically, a narrow band method is employed to solve Equation (23). The main steps are summarized as follows:

Algorithm Narrow band for the Geometric Active Contour

1: Initialize the level set function U with C_0
2: Construct a narrow band $\Omega_{M_{bp}}$ around the current contour on M_{bp}
3: Update U in $\Omega_{M_{bp}}$, according to

$$U(p, t+1) = U(p, t) + dt \left(|\nabla_{M_{bp}} U|\nabla_{M_{bp}} \cdot \left(g\frac{\nabla_{M_{bp}} U}{|\nabla_{M_{bp}} U|} \right) \right)_{(p,t)}, \tag{24}$$

where dt is the time step in discretizing U
4: Find the new zero level set of U to update the contour C
5: Repeat steps 2-4 until it converges or reaches the maximum number of iterations

In step 1, U is realized as the signed distance function from C_0, which decomposes M_{bp} into several regions. The sign of U is positive in the region that contains the apex point. The fast marching method is used to build $\Omega_{M_{bp}}$ from C_0 with a threshold

ϕ_{max} to control the size of the narrow band. Typically, set $\phi_{max} = \min(10, 4l_{max})$ mm, where l_{max} is the length of the longest edge on M_{bp}.

Step 3 requires numerical approximations for gradient and divergence operators on a surface. The discretization schemes of [50] were adopted because they naturally capture the geometric properties of surfaces. Note that the surface M_{bp} is represented by a triangle mesh as $M_{bp} = \{V = \{p_i\}_{i=1}^{N}, T = \{T_k\}_{k=1}^{L}\}$, where $p_i \in \mathbb{R}^3$ is the ith vertex and T_k represents the kth triangle. The surface gradient and divergence operators at a vertex are approximated by taking the weighted average of the discretized operators over the first-ring neighbors of the vertex.

Let $f = \{f(p_1), f(p_2), f(p_3)\}$ be a function and $\mathbf{V} = \{\mathbf{V}(p_1), \mathbf{V}(p_2), \mathbf{V}(p_3)\}$ a vector field defined at each vertex. For any point p inside T_k, the values of f and $\mathbf{V}$ can be interpolated as

$$\begin{cases} p = \chi^1(p_1 - p_3) + \chi^2(p_2 - p_3) + p_3 \\ f(p) = \chi^1(f(p_1) - f(p_3)) + \chi^2(f(p_2) - f(p_3)) + f(p_3) \\ \mathbf{V}(p) = \chi^1(\mathbf{V}(p_1) - \mathbf{V}(p_3)) + \chi^2(\mathbf{V}(p_2) - \mathbf{V}(p_3)) + \mathbf{V}(p_3) \end{cases} \tag{25}$$

where $(\chi^1, \chi^2, 1 - \chi^1 - \chi^2)$ is the barycentric coordinate of T_k. Here, $\chi = (\chi^1, \chi^2)$ defines a local coordinate system for M_{bp}. Then the approximations of these two operators are

$$\nabla_M f(p_i) = \frac{1}{\sum_l Area(T_l)} \sum_l Area(T_l) \nabla_{T_l} f(p_i) \tag{26}$$

$$\nabla_M \cdot \mathbf{V}(p_i) = \frac{1}{\sum_l Area(T_l)} \sum_l Area(T_l) \nabla_{T_l} \cdot \mathbf{V}(p_i), \tag{27}$$

where l traces through all triangles in the first ring of the vertex p_i to average the discretized operators at each vertex (see Appendix A for details). The time step of $dt = 1$ was used in implementation.

In step 4, a new zero level set is obtained from U. The algorithm stops either when the contour stops evolution or the maximum number of iterations is reached.

To reduce the effect of local noise (see Figure 6(a)), the contour evolution process described above may be applied twice. In the first round, set $g = 1$ so that it shortens the initial contour by its geometric curvature flow. Then, the feature function defined in Equation (21) is utilized to refine the contour so that it stops at locally concave locations. Finally, the endocardial surface, denoted by M_{endo}, is extracted, which is separated by the cut contour from other regions on M_{bp}. An illustration of the LV localization process is shown in Figure 6. In this figure, an initial cut contour C_0 starts from a location away from expected location. Being attracted by the gradient descent flows, it moves towards the expected location and finally stops at there.

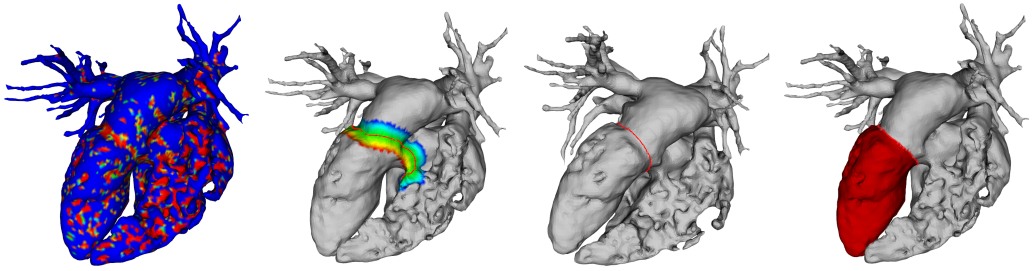

(a) (b) (c) (d)

Figure 6: The LV localization. (a) Features on surface M_{bp}. (b) The initial contour C_0 and its narrow band $\Omega_{M_{bp}}$. (c) Final contour C_{lv}. (d) Segmented endocardial surface.

2.2.1.5 Extract the LV Endocardium

The endocardial surface M^{lv}_{endo} is closed by triangulating the points along the cut contour C_{lv}. Here, M^{lv}_{endo} is still used to denote the closed surface. Then, M^{lv}_{endo} is rasterized to get a mask image $\tilde{I}^{lv}_{endo}$, which has the same origin and resolution as the source image I. To remove noise and papillary muscles, the convex hull of M^{lv}_{endo} is constructed and set as the ROI for performing the morphological closing operation on $\tilde{I}^{lv}_{endo}$. The size of the structure element for the closing operator depends on the size of the papillary muscles, which was empirically set as 3 mm. An example of papillary muscle removal is shown in Figure 7.

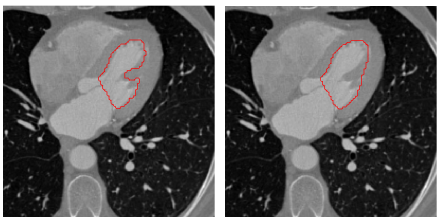

(a) (b)

Figure 7: Segmentation of the endocardium (red) (a) before and (b) after removing the papillary muscles.

2.2.1.6 Segment the LV Epicardium

One way of initializing the epicardial mask is by dilating the endocardium to a given distance. For example, the elements of $\tilde{I}^{lv}_{epi}$ can determined by choosing voxels within a certain distance range to the $\tilde{I}^{lv}_{endo}$ boundary. This works well for a myocardial wall with a nearly uniform thickness. Here, another way is proposed to initialize $\tilde{I}^{lv}_{epi}$ by utilizing a variational region-growing method that is driven by the robust statistics of image intensities. Similar as in the dilation-based methods, a distance field from $\tilde{I}^{lv}_{endo}$ is computed and a small strip region that lies between d_{in} and d_{out} away is chosen as the seed region for the epicardial mask. Typically, the values are set to $d_{in} = 2$ mm and $d_{out} = 4$ mm. The blood pool voxels are excluded from this region. Once a seed region of the epicardial mask is determined, the robust-statistics-based energy functional [33] is then defined as

$$E_{\mathrm{RS}}(\phi) = \lambda_{RS} \int_{\Omega} -p(\boldsymbol{f}(x))H(\phi(x))dx + (1-\lambda_{RS}) \int_{\Omega} \delta(x)|\nabla\phi(x)|dx, \qquad (28)$$

where ϕ is the signed distance function from the epicardial mask, and H is the Heaviside function. Here, $p(\boldsymbol{f}(x))$ is the probability density function of a feature vector $\boldsymbol{f}(x)$ that evaluates the intensity median, inter-quartile range, and median absolute deviation, respectively, around a neighborhood of a point $x \in \Omega$. This probability function $p(\boldsymbol{f}(x))$ can be learned from the intensities inside the seed region via kernel regression. The first term in this equation measures the intensity homogeneity inside the contour, and the second term is the length of the contour that controls

the smoothness of the final result. In implementation, λ_{RS} was empirically set as $\lambda_{RS} = 0.2$. The gradient descent flow of $E_{RS}(\phi)$ with respect to ϕ is

$$\frac{\partial \phi(x)}{\partial t} = \lambda_{RS}\delta(\phi(x))p(\boldsymbol{f}(x)) + (1-\lambda_{RS})|\nabla\phi(x)|\nabla\cdot\Big(\frac{\nabla\phi(x)}{|\nabla\phi(x)|}\Big). \tag{29}$$

In practice, a parameter d_w is used to control the maximum distance allowed in the region-growing process. The value of this parameter is related to the average thickness of the myocardial wall, which typically ranges from 6 to 16 mm [67]. In all of experiments, d_w was empirically set as $d_w = 16$ mm.

The myocardial masks, $\tilde{I}^{lv}_{epi}$ and $\tilde{I}^{lv}_{end}$, provide a good localization of the epicardium and endocardium, which impose a shape constraint for local refinement, especially on regions of low contrast or poor edges.

2.2.2 Right Ventricle Localization

The same strategy is used to localize the RV. In particular, the RV region is identified on the heart surface reconstructed by utilizing a variational region-growing method. The location of the LV is used to infer the initial location of the cut contour for the RV. Given a seed region extracted based on the RV localization result,the region-growing method is employed to extract a smooth epicardial mask of the RV.

2.2.2.1 Reconstruct the Heart Surface

The intensity inside the RV blood pool may not be as homogeneous as that of the LV. To identify the RV, a smooth heart surface is reconstructed by taking the LV endocardium as a seed region to start a variational region-growing process. In implementation, the parameter λ_{RS} was empirically set as $\lambda_{RS} = 0.9$ so that the intensity homogeneity force term plays a leading role while competing with the smoothing energy to explore the entire heart region. The surface is represented as a triangulated surface, denoted by M_{ht}. An example of the region-growing process is shown in Figure 8. Note that a major portion of the LV endocardium is the blood pool and a minor

the papillary muscles (see Figure 8(a)). Thus, as illustrated by Figures 8(b) and 8(c), the growing process shows a higher priority to expand brighter regions than the dark ones. Combing the effect of the smoothing term, the growing process gradually captures a smooth heart region.

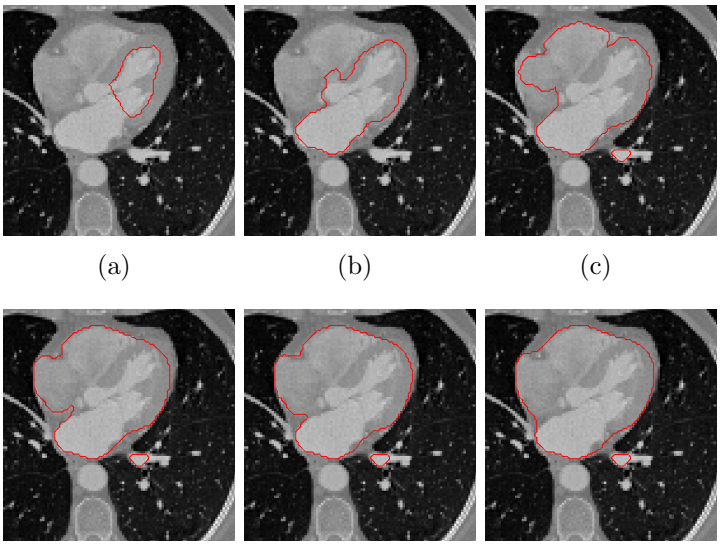

Figure 8: Variational region-growing process for segmenting the heart surface.

2.2.2.2 Find an Initial Cut Contour

The closest point from M_{ht} to the LV apex p_{apx} is used as a starting point to reconstruct the distance field on M_{ht}. Then, the distance field is sampled evenly at an interval of 2 mm. Let $\{\tilde{p}_i\}, i = 1 \cdots m$, be the points of a given isocontour C. The distance between the isocontour and the cut contour C_{lv} of M_{bp} is approximated by

$$d(C, C_{lv}) = \frac{1}{m} \sum_{i=1}^{m} |\mathbf{N}_{lv} \cdot (\tilde{p}_i - p_c)|, \tag{30}$$

where $\mathbf{N}_{lv}$ and p_c are the unit normal of the best fitting plane and centroid of C_{lv}, respectively. Then, the isocontour with the minimal distance to C_{lv} is selected as the initial contour that identifies the ventricles on M_{ht}.

2.2.2.3 Segment the RV Endocardium

The initial cut contour C_{vs}^0 is refined by using the geometric active contour model described in Section 2.2.1.4. The surface determined by C_{vs} includes both the LV and RV, which is rasterized to get a mask for the ventricles, denoted by $\tilde{I}_{vs}$. To extract the endocardial mask of the RV, the voxels belonging to the LV and blood pool are excluded from $\tilde{I}_{vs}$. Figure 9 shows the process of segmenting the the RV endocardium.

(a) (b) (c) (d)

Figure 9: Segmentation of the RV endocardium. (a) The initial contour C_{vs}^0 and its narrow band. (b) The ventricles (red) determined by C_{vs} on the heart surface M_{ht}. (c) The ventricles in the source image. (d) The extract RV endcardium.

2.2.2.4 Segment the RV Epicardium

The same procedure as in 2.2.1.6 is applied to generate the RV epicardial mask $\tilde{I}_{epi}^{rv}$. Typically, the seed region is controlled by $d_{out} = 2$ mm and $d_{out} = 3$ mm for $\tilde{I}_{epi}^{rv}$, and the maximum allowed distance is set as $d_w = 5$ mm for the RV.

2.2.3 Myocardial Wall Extraction

To extract the myocardial wall, the mask images of the ventricles are refined by employing an active contour method with a shape constraint that allows local variations around the segmented masks. After that, the outlier voxels are excluded to get a complete wall structure.

2.2.3.1 *Refine the Myocardial Masks*

Given a mask image $\tilde{I} \in \{\tilde{I}^{lv}_{endo}, \tilde{I}^{rv}_{endo}, \tilde{I}^{lv}_{epi}, \tilde{I}^{rv}_{epi}\}$ of a myocardial surface, the energy functional for refining the mask image is designed as

$$\begin{aligned} E(\phi) =& \lambda \int_{\Omega_x} \delta(\phi(x)) \int_{\Omega_y} B(x,y) F(I(y), \phi(y)) dy dx \\ &+ (1-\lambda) \int_{\Omega} \tilde{g}(\tilde{\phi}(x)) \delta(x) |\nabla \phi(x)| dx \end{aligned}, \tag{31}$$

where $B(x,y)$ is a characteristic function of radius r for any $x, y \in \Omega$

$$B(x,y) = \begin{cases} 1 & \| x-y \| < r \\ 0 & \text{otherwise} \end{cases}, \tag{32}$$

and $\tilde{g} : \mathbb{R} \rightarrow \mathbb{R}^+$ is a feature function that imposes the shape constraint,

$$\tilde{g}(\tilde{\phi}) = (d_{max} - d_{min}) \Big(1 + exp\Big(\frac{-|\tilde{\phi}| - \beta}{\alpha}\Big)\Big)^{-1} + d_{min}. \tag{33}$$

An example of the shape of the feature function is shown in Figure 10. The term

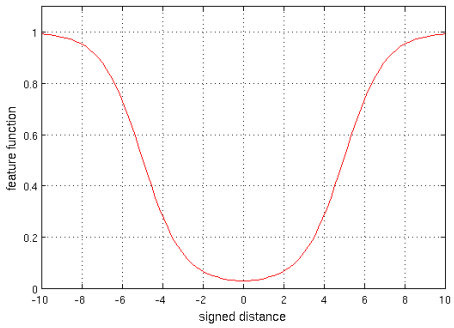

Figure 10: Feature function $\tilde{g}(\tilde{\phi})$ with $\alpha = 1$, $\beta = 5$, $d_{max} = 1$ mm and $d_{min} = 0.02$ mm.

$F(I(y), \phi(y))$ is a generic internal energy term defined over Ω. In this work, a localized Chan-Vese energy [14, 52] is used,

$$F(I(y), \phi(y)) = H(\phi(y))(I(y) - u_x)^2 + (1 - H(\phi(y))(I(y) - v_x)^2, \tag{34}$$

where u_x and v_x are the local means defined in terms of $B(x,y)$ as

$$u_x = \frac{\int_{\Omega_y} B(x,y) H(\phi(y)) I(y) dy}{\int_{\Omega_y} B(x,y) H(\phi(y)) dy}, \tag{35}$$

$$v_x = \frac{\int_{\Omega_y} B(x,y)(1-H(\phi(y)))I(y)dy}{\int_{\Omega_y} B(x,y)(1-H(\phi(y)))dy}. \tag{36}$$

The first term in Equation (31) is a localized region-based energy [52] that combines the advantages of the edge- and region-based active contour models. The second term is essentially the geometric active contour energy [48, 13] that uses the feature image $\tilde{g}$ to prevent the contour from drifting away from its initial location. The gradient descent flow of $E(\phi)$ is

$$\begin{aligned}\frac{\partial \phi(x)}{\partial t} = {} & \lambda\delta(\phi(x)) \int_{\Omega_y} B(x,y)\delta(\phi(y)) \cdot (-(I(y)-u_x)^2 + (I(y)-v_x)^2)dy \\ & + (1-\lambda)\Big(\tilde{g}|\nabla\phi|\nabla\cdot\Big(\frac{\nabla\phi}{|\nabla\phi|}\Big) + \xi\tilde{g}|\nabla\phi| \ + \nabla\tilde{g}\cdot\nabla\phi\Big)(x)\end{aligned} \quad . \tag{37}$$

An extra term, $\xi\tilde{g}|\nabla\phi|$, is used to increase the convergence speed and facilitate the detection of non-convex boundaries [4]. In implementation, ξ was set to $\xi = 1$.

The sparse level set method [82] was utilized to implement the active contour model for its efficiency. In particular, the upwind scheme was used in discretizing $|\nabla(\cdot)|$ (see [4] for details). The endocardial and epicardial masks were refined separately. The radius of the characteristic function $B(x,y)$ defined in Equation (32) was set as $r = 4$ mm.

2.2.3.2 Extract the Myocardial Wall

The myocardial wall is defined as the volume between the endocardial and epicardial masks. The majority of the wall can be determined by performing the logic XOR operation between the endocardial and epicardial masks of the LV and RV, respectively. Note that the contour evolution process returns closed surfaces. Thus, the voxels inside the blood pool are excluded to extract a complete myocardial wall. An example of extracting the myocardial wall is given in Figure 11. It is clear that, by using the procedure described above, smooth endocardial masks are extracted in the presence of noise and papillary muscles. Further, the epicardial masks are separated from the background with soft tissues around the apex point and cut off at the right

place including the top. The use of the shape constraint makes the evolution process go smoothly while preserving the overall shape as well as adapting to local image content.

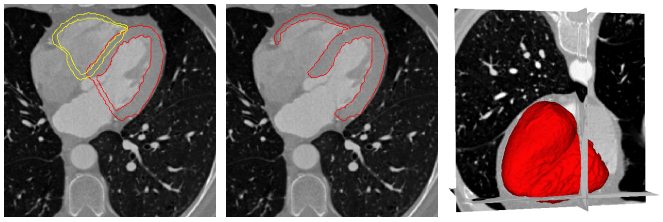

(a) (b) (c)

Figure 11: Segmentation of the myocardial wall. (a) Refined myocardial masks. (b) Extracted myocardial wall. (c) The wall in a 3D view.

2.3 Experimental Results

This study was approved by the Institutional Review Board. The robustness and accuracy of the proposed method were tested on 30 human and 12 pig cardiac CT images. For the human data, the in-slice resolution is 256×256 with the number of slices varying from 138 to 220, or 512×512 with slice number ranging from 137 to 293. The voxel size varies from $0.54 \times 0.54 \times 0.54$ mm^3 to $0.81 \times 0.81 \times 0.81$ mm^3 for the first case, and $0.39 \times 0.39 \times 0.50$ mm^3 to $0.58 \times 0.58 \times 0.40$ mm^3 for the second. The human dataset include anomaly cases (hypertrophic cardiomyopathy where the myocardium is hypertrophied and aneurysm with abnormally enlarged aorta region) and volumes with different scanning quality. All of the pig data have the same voxel size of $1.0 \times 1.0 \times 1.0$ mm^3 with resolution varying from $116 \times 116 \times 108$ to $257 \times 257 \times 220$.

2.3.1 Implementation

The overall framework was implemented in C++. An open source package ITK [34] was used for basic image processing tasks such as morphological and logic operations, conversion between triangle mesh and image volume. The convex hull extraction and

3D visualization were realized using VTK [81].

In extracting the blood pool, the source image was downsampled to a voxel resolution of $2.0 \times 2.0 \times 2.0$ mm^3. The shape of the LV is well preserved at this resolution. The thresholds of 180 and 350 in Hounsfield units were used for the human and pig datasets, respectively, so that the left and right ventricles can be separated after thresholding.

2.3.2 Robustness Test

The robustness of two important steps, the LV localization and the epicardium initialization, were analyzed. To test the robustness of LV localization described in Section 2.2.1, sample points randomly selected from a neighborhood within 30 mm of the apex point were used as trial apex points to start the localization process. To quantify errors, the distance between the original cut contour and the one generated from one of those sample points was measured as

$$d(C, \tilde{C}) = \frac{\int_{\tilde{C}(s)} D(C) ds}{\int_{\tilde{C}(s) ds}}. \tag{38}$$

Here, C is the original cut contour, D is the distance field starting from C, and $\tilde{C}$ is the cut contour obtained from a sample point. In implementation, $D(C)$ was evaluated at triangle vertices. The initial and final errors $d(C, \tilde{C})$ for 20 randomly sampled points is shown in Figure 12. All of the cut contours generated with the sampled apex points converge to the original C with a tolerable numerical error. In addition, the average of the turning points $\tilde{d}$ in initializing the cut contours were 94 ± 9 mm and 76 ± 6 mm for the human and pig datasets, respectively. This result shows that the features used for identifying the cut contour is stable in presence of heart shape variability.

Similarly, the sensitivity of the epicardium initialization method to the maximal allowed myocardial thickness d_w was examined by measuring the average point-to-surface distance between the surfaces obtained with varying d_w and the one with a

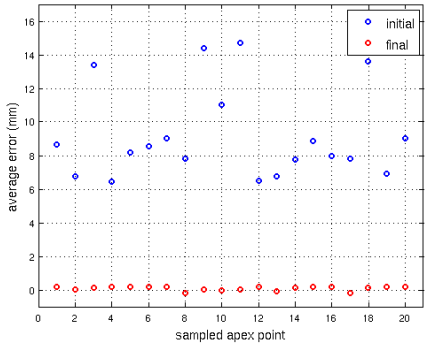

Figure 12: Initial and find errors for the cut contours generated from 20 randomly sampled apex points.

fixed d_w. One example, using the initialized epicardium extracted at $d_w = 16$ mm as a reference, is shown in Figure 13. It shows that the localization method is stable for $d_w > 16$ mm, which agrees with the thickness of a normal myocardial wall [67].

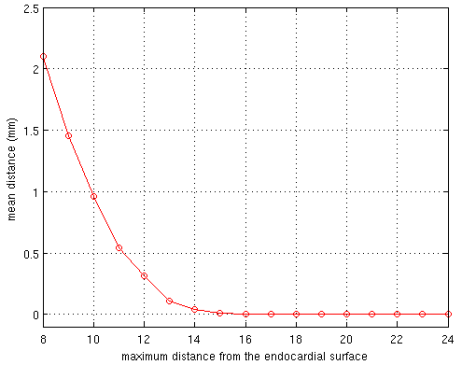

Figure 13: Average distance from epicardial masks to a reference one with varying maximal allowed myocardial thickness d_w.

The proposed method succeeded in localizing the LV and RV for all of the testing datasets with wide shape variations and different volume coverages. Two examples of segmentation for the human dataset with significantly different heart shapes are presented in Figure 14. The results of pig dataset with different volume coverages are shown in Figure 15. As indicated by these results, the papillary muscles, pericardium, and soft tissues were successfully excluded from the myocardium.

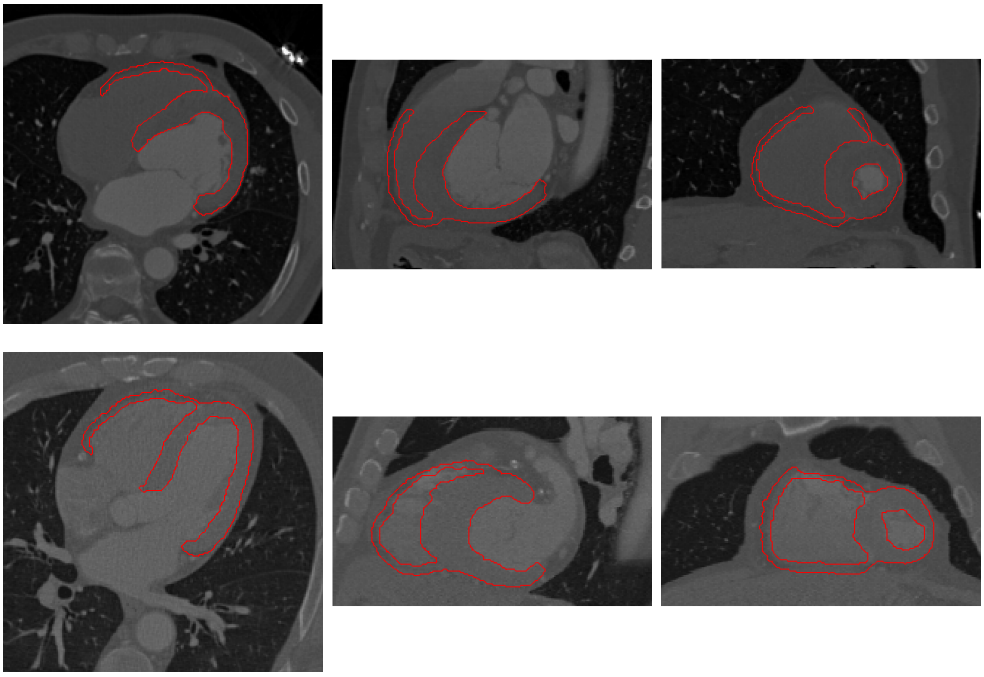

Figure 14: Myocardium segmentation results of human data with significantly different heart shapes. From left to right are myocardial wall in axial, coronal, and sagittal views, respectively.

2.3.3 Quantitative Analysis

To make a fair comparison, all testing datasets were resampled to the same resolution of the manual segmentations at $1.0 \times 1.0 \times 1.0$ mm^3. The mean and standard deviation of the point-to-surface errors for the human and pig datasets at the localization and refinement steps are shown in Table 1. These results show that the localization step locates the endocardial and epicardial masks with high precision as compared to the manual segmentations, which are further refined by applying the active contour model with the shape constraint. Note that the accuracy of the endocardium segmentation is better than the epicardium segmentation as the former is better defined because of the high contrast between the blood pool and the myocardium, while in the latter case poor contrast and weak edges are present between the epicardium and background tissues.

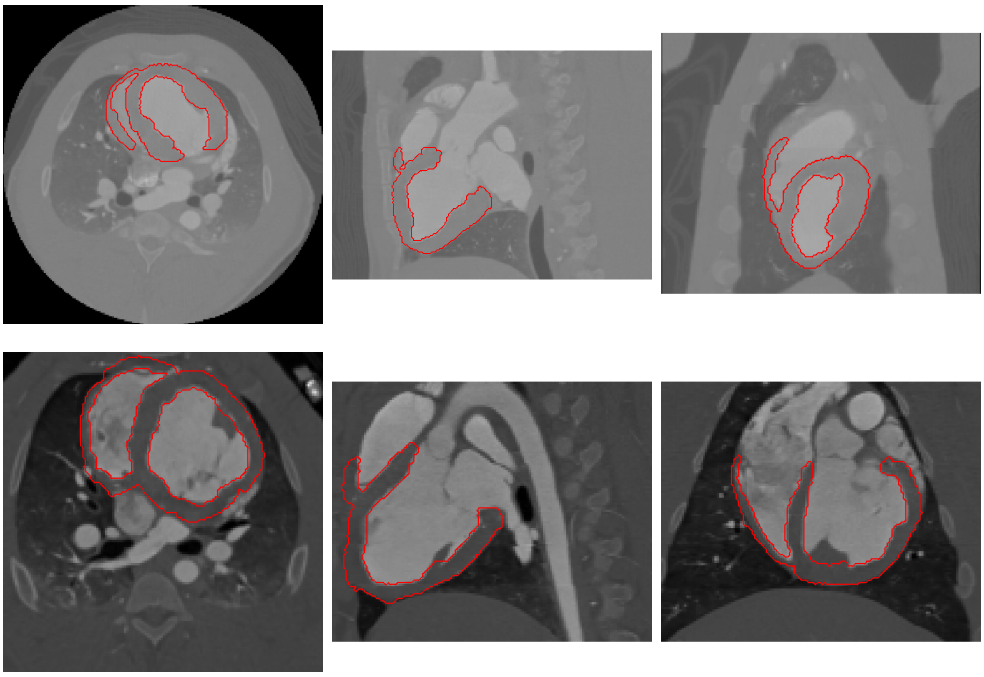

Figure 15: Myocardium segmentation results of pig data with different volume coverages. From left to right are the myocardial wall in axial, coronal, and sagittal views, respectively.

In addition, the proposed method was compared to a state-of-the-art active contour method, *i.e.*, localized PCA-based method [1, 2], for segmenting pig ventricles using the same dataset. As shown in Table 2, the proposed method has a higher accuracy as it captures more local image content than the PCA-based method, which relies on the sub-space where the heart shape is embedded.

Though it is hard to make a fair comparison between different methods for human ventricle segmentation by using different datasets, the accuracy of the proposed method seems to be competitive with some latest results: 1.13 ± 0.55 and 1.21 ± 0.41 mm [89], 0.98 ± 1.32 and 0.82 ± 1.07 mm [25] for LV endocardium and epicardium, respectively. Note that, the comparison is only made to the LV segmentation because the approaches being compared with model the RV endocardium and epicardium as a single component.

To evaluate the time complexity, the proposed method was tested on a computer

Table 1: Mean and standard deviation of the point-to-surface errors in localization and refinement (in mm).

Data	Stages	LV-Endo	LV-Epi	RV-Endo	RV-Epi
Human	Localization	1.05 ± 1.00	1.25 ± 1.21	1.66 ± 1.77	1.98 ± 1.91
	Refinement	0.87 ± 0.94	1.06 ± 1.15	1.46 ± 1.63	1.57 ± 1.78
Pig	Localization	0.83 ± 0.89	1.05 ± 1.12	1.31 ± 1.43	1.78 ± 1.70
	Refinement	0.72 ± 0.88	0.80 ± 0.99	1.28 ± 1.40	1.32 ± 1.64

Table 2: Comparison between the proposed method and localized PCA for the segmentation of pig ventricles(in mm).

Method	LV-Endo	LV-Epi	RV-Endo	RV-Epi
Proposed method	0.72 ± 0.88	0.80 ± 0.99	1.28 ± 1.40	1.32 ± 1.64
Local-PCA	1.08 ± 1.12	1.10 ± 1.40	1.58 ± 1.71	1.61 ± 1.96

with Quad CPU 3GHz, 8G RAM. The average processing time for the LV segmentation is presented in Table 3.

Table 3: Average computation time for the LV segmentation(in seconds).

	Human	Pig
Localization	25.2	15.6
Refinement	61.6	41.6
Total	89.0	58.1

Given the mask of the LV myocardium wall, the volume enclosed by the wall can be computed by using the same computational method as in [93]. The mass of the LV was computed as the product of the volume and density, where the density $\rho = 1.05$g/mL in experiments. For the human dataset, the average absolute difference between the masses from automatic and manual segmentations was 7.8 ± 5.0g, which is $5.5\% \pm 3.5\%$ with respect to the mean mass. For the pig dataset, this difference was 4.2 ± 2.9g, which accounts for $6.4\% \pm 4.4\%$ of the mean mass.

2.4 Conclusion

This chapter has presented an automatic method for segmenting the ventricles from cardiac CT images. The method sequentially segments the LV and RV via integrating

shape segmentation with region-growing techniques. In particular, each ventricle is detected by first identifying the endocardium and then segmenting the epicardium. In addition, the LV segmentation results are used to localize the RV. The local variations of the heart are naturally handled by utilizing features obtained online. Its performance has been evaluated by measuring the errors between automatic and manual segmentations. In these tests, the proposed method achieves high accuracy as well as strong robustness for segmenting the myocardial wall from both human and datasets with large shape variabilities and different volume coverages. In future work, we plan to apply the segmentations from the proposed approach to clinical applications such as evaluating the myocardial mass at risk caused by stenoses.

CHAPTER III

SEGMENTATION OF THE LEFT ATRIUM FROM MR IMAGES

In this Chapter, an effective method is proposed to segment the LA from MR images. The segmentation is formulated in the framework of variational region growing. Specifically, the method begins by searching for a seed region of the LA from a slice of an image. Then, a shape prior is integrated into the growing process to account for data variations such as sharp LA shape differences, wide volume coverages, and different image qualities. The details of the method is presented in th following sections.

3.1 Proposed Method

The proposed method consists of two key steps: (1) search for a seed region of the LA from an image slice in the axial view. (2) explore the LA region using a variational region-growing process. A shape prior is employed to drive the growing process towards atrium-like shapes.

3.1.1 Seed Region Extraction

In region-growing, it is common to initialize the seed region close to the center of the target to be segmented. In our case, one feature that can be used for this purpose is based on the spatial relationship between the LA and LV. Specifically, as shown in Figure 16, the relative size between the LA and LV in an axial view indicates the *centrality* of a slice with respect to the LA without going through all of image slices. Based on this observation, the seed region extraction process begins by searching for the LA and LV regions from the middle slice of an MRI image. Then, the "centrality"

of the current slice with respect to the LA is evaluated. If this value is greater than a predefined threshold, one goes to next slice and repeats the process until a proper slice is found.

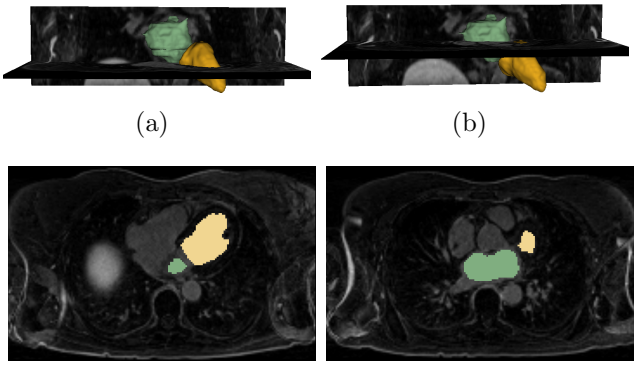

Figure 16: Spatial relationship between the LA (green) and LV (brown). (a)(c) 2D and 3D views at the bottom of the LA. (b)(d) 2D and 3D views at the central of LA.

3.1.1.1 Heart Region Detection

An active contour model is employed to segment the heart region that contains the LA and LV regions. Let $I_i \in \mathbb{R}^2$ be the current slice. Since the heart region has higher intensity values than its surrounding structures (such as the lungs), I_i may be thresholded to highlight these brighter regions. The threshold is determined as

$$T_{heart} = \min\{T_{\text{global}}, T_{\text{local}}\}, \tag{39}$$

where T_{global} is the intensity value returned by the method in [64] that gives the best separation of the image histogram over the slice, and T_{local} is the mean intensity of a region with a high probability of containing the LA which is learned from training images. This thresholding strategy reduces the possibility of missing the heart region while only the global threshold T_{global} is used when the liver or thoracic wall has very high intensities. After applying a morphological opening operator to remove noisy structures, the connected components $\{L_k\}$ of the thresholded image are labeled. A

measurement is associated with each connected component L_k as follows

$$h(L_k, P_c) = \frac{A(L_k)}{d(L_k, P_c)}, \tag{40}$$

where $A(L_k)$ is the area of component L_k, and $d(L_k, P_c)$ is the Euclidean distance from the center of this component to the slice center P_c. This measurement favors large regions with small distance to the center of the slice. The one with the largest $h(L_k, P_c)$ value is chosen as a coarse segmentation of the heart region.

Let $\phi : \Omega_p \to \mathbb{R}$ denote the signed distance function of a contour defined over the image domain $\Omega_p \in \mathbb{R}^2$ with positive distances inside and negative distances otherwise. The coarse segmentation is refined by using a localized region-based active contour method [52, 51] to minimize the energy functional

$$E(\phi) = \int_{\Omega_p} \delta(\phi(p)) \int_{\Omega_q} B(p,q) F(I(q), \phi(q)) dq dp + \lambda \int_{\Omega_p} \delta(\phi(p)) |\nabla \phi(p)| dp \tag{41}$$

where the second term is a regularization term that measures the length of a contour. Here, $F(I(q), \phi(q))$ is a generic internal energy term defined over Ω_q. In this work, a localized Chan-Vese energy [14, 52] is used,

$$F(I(q), \phi(q)) = H(\phi(q))(I(q) - u_p)^2 + (1 - H(\phi(q))(I(q) - v_p)^2, \tag{42}$$

where u_p and v_p are the local means defined in terms of a ball structure $B(p,q)$ centered at p with radius R as

$$u_p = \frac{\int_{\Omega_q} B(p,q) H(\phi(q)) I(q) dq}{\int_{\Omega_q} B(p,q) H(\phi(q)) q}, \tag{43}$$

$$v_p = \frac{\int_{\Omega_q} B(p,q)(1 - H(\phi(q))) I(y) dq}{\int_{\Omega_q} B(p,q)(1 - H(\phi(q))) dq}, \tag{44}$$

and H is the Heaviside function

$$H(z) = \begin{cases} 1 & \text{if } z \geq 0 \\ 0 & \text{if } z < 0 \end{cases}. \tag{45}$$

The gradient descent flow of $E(\phi)$ is

$$\begin{aligned}\frac{\partial \phi(p)}{\partial t} =& \delta(\phi(p))\Big(\int_{\Omega_q} B(p,q)\delta(\phi(q))\cdot(-(I(q)-u_p)^2+(I(q)-v_p)^2)dq\Big)(p) \\ &+ \lambda|\nabla\phi|\nabla\cdot\Big(\frac{\nabla\phi}{|\nabla\phi|}\Big)(p)\end{aligned} \quad . \tag{46}$$

3.1.1.2 Seed Region Extraction

Suppose the origin of I_i is at the top left corner of the image with horizontal as the first component and vertical second, and denoted any point on I_i as (p^1, p^2). Let the mask of the heart region be $I_{\text{heart}} \in \{0, 1\}$. Note that, as illustrated by Figure 16(d), two observations facilitate the detection of the LA: First, the LA region has relative larger p^2 component as compared with other points inside I_{heart}. Second, partial edges exist that distinguish the LA from other heart chambers. Therefore, the gradient information of I_i is used to narrow down the search space of the LA seed. In particular, I_{heart} is used as the region of interest (ROI) for the following operations to extract a seed region.

To begin with, the magnitude of the gradient of I_i is computed, which is then thresholded using the mean gradient as a threshold. After that, an edge map I_{edge} of this binarized image is obtained by applying a binary thinning operation. Next, a distance field image I_{dist} is reconstructed by performing distance transform [10] on the edge image. Finally, a candidate seed region is detected by searching for a circular region $S_{\text{LA}}(p, r)$ that maximizes the following measurement:

$$S_{\text{LA}}(p, r) = \frac{\int_{B(p,r)} I_{\text{dist}}(p)dA}{d(p, P_{ref})} \tag{47}$$

where $B(p, r)$ is a ball of radius r centered at p, and $d(p, P_{ref})$ is the Euclidean distance from $p = (p^1, p^2)$ to a reference point $P_{ref} = (p^1_{ref}, p^2_{ref})$ with

$$\begin{cases} p^1_{ref} = \text{mean}_{p_1}\{I_{heart}(p)\} \\ p^2_{ref} = \max_{p_2}\{I_{heart}(p)\} + t_{ref} \end{cases} , \tag{48}$$

where t_{ref} is a constant to avoid numerical singularity.

3.1.1.3 Slice Centralization

To check whether the current slice I_i is approximately centralized with respect to the LA, the areas of the LA and LV need to be determined. To this end, a morphological opening operator is performed on the distance image I_{dist} to isolate the LA region from the other chambers, which returns a group of connected regions. The one containing S_{LA} is selected as the mask of the LA, denoted by I_{LA} .

The determination of the LV region is based on the fact that it resides to the top right of LA as shown in Figure 16(c). Thus, the centroid of S_{LA} is used as a reference origin, with respect to which to divide the top right quadrant equally into two sections; see Figure 17(d). In each of these two sections, the closest points along the contour of I_{heart} is searched and used as the starting and ending points for the LV. Connecting these two points with the centroid of I_{LA} gives a ROI of the LV. The LV region, denoted by I_{LV}, is extracted by removing the points of I_{LA} from the ROI. The centrality of the slice I_i with respect to the LA is defined as

$$g = \frac{A(I_{\text{LV}})}{A(I_{\text{LA}})} \max_p d(I_{\text{LV}}(p), I_{\text{LA}}), \tag{49}$$

where $A(\cdot)$ is the area of a mask, and $d(I_{\text{LV}}(p), I_{\text{LA}})$ is the Euclidean distance from a point p to I_{LA}. The first part of Equation (49) evaluates the significance of the LV with respect to the LA, and the second part gives the largest distance from the LV mask to the LA mask. The values of these two parts are expected to be small if the slice I_i is close to the center of the LA, which can be controlled by a threshold t_{LA} learned from training images. Once the seed region is identified, its size is adjusted so that $r^* = \max_r I_{dist}(p) > 0$ for $\forall p \in S_{\text{LA}}(p, r)$.

Figure 17 illustrates the process of detecting a seed region. Note that, although the boundaries are not clearly defined at where the LA merges into other chambers, partial boundaries still exist that separate the LA from other heart regions. Specifically, as shown in Figure 17(c), a distinct cluster containing the LA is formed. Thus, the

seed region was successfully identified using the measurement defined in Equation 47. Finally, the centralized slice was found with correctly detected seed region as in Figure 17(f).

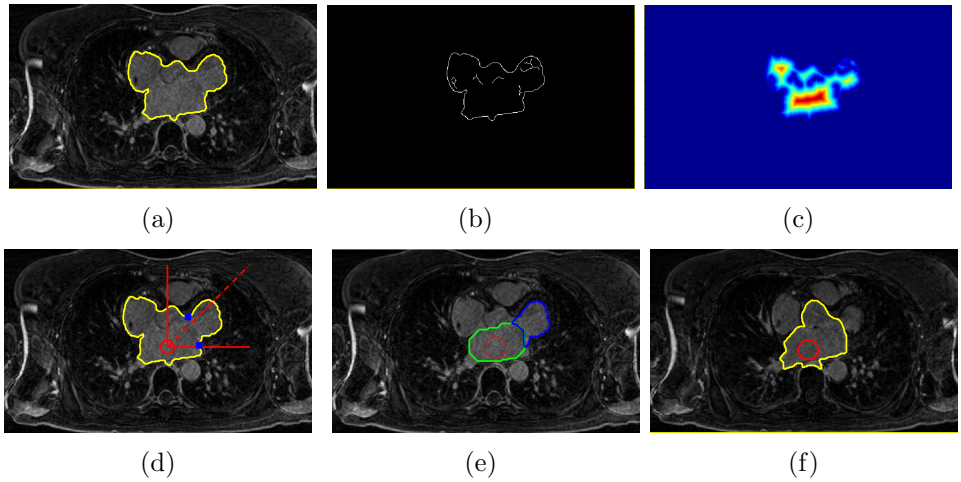

Figure 17: Seed region detection process. (a). Heart region segmentation (yellow contour). (b) Edges within the heart region. (c) Distance field. (d) Starting and ending points (blue) for the LV region. (e) Extraction of masks of the LV (blue) and LA (green). (f) The seed region (red circle) in the centralized slice.

3.1.2 Variational Region Growing with a Shape Prior

Given a properly set seed region, a growing process driven by the robust statistics of the seed region is employed to explore the entire LA region. However, leakage is almost inevitable because the statistics computed does not provide a global shape constraint on evolving contours. Hence, a shape prior is applied to attract the growing process towards an expected shape. The details of how to integrate this prior information into the growing process is described in the following sections.

3.1.2.1 Variational Region Growing

Given a seed region, the variational region-growing model [33] explores homogeneous regions under a given geometric constraint. Robust statistics of intensities are evaluated to measure the homogeneity among neighboring voxels. To this end, a feature

vector is defined for each voxel $\boldsymbol{x} = (x, y, z) \in \mathbb{R}^3$ in an image as

$$\boldsymbol{f}(\boldsymbol{x}) = (MED(\boldsymbol{x}), IQR(\boldsymbol{x})), MAD(\boldsymbol{x}))^T \in \mathbb{R}^3, \tag{50}$$

where $MED(\boldsymbol{x})$, $IQR(\boldsymbol{x})$, and $MAD(\boldsymbol{x})$ are the intensity median, inter-quartile range, and median absolute deviation around a neighborhood of $\boldsymbol{x}$, respectively. Then, the seed region is characterized by the probability density function of the feature vectors as

$$p(\boldsymbol{f}) = \frac{1}{|G|} \sum_{x \in G} K_\eta(\boldsymbol{f} - \boldsymbol{f}(\boldsymbol{x})), \tag{51}$$

where K is the kernel function. A Gaussian kernel is used in this work. The kernel width, denoted by t_g, controls the intensity homogeneity favored by the growing process. The region-growing energy functional is defined as

$$E_{\mathrm{RS}}(\phi) = \int_\Omega -p(\boldsymbol{f}(\boldsymbol{x}))H(\phi(\boldsymbol{x}))d\boldsymbol{x}, \tag{52}$$

which evaluates the intensity homogeneity inside a contour where $\phi > 0$.

The gradient descent flow of $E_{RS}(\phi)$ with respect to ϕ is

$$\frac{\partial E_{\mathrm{RS}}}{\partial \phi} = \delta(\phi(\boldsymbol{x}))p(\boldsymbol{f}(\boldsymbol{x})). \tag{53}$$

This flow captures homogeneous regions based on the statistics from the seed region. We should note that a regularization term is typically used to balance the growing force so that the evolution stops at the expected position.

3.1.2.2 Zernike Moments as a Shape Prior

Note that the flow in Equation (53) only involves a local computation. Thus, the growing process tends to leak into homogeneous regions with poor boundaries if there is not some global constraint over the evolving shape.

The Zernike moments are many times used as a shape descriptor because of their invariance to translation, rotation, and scaling. The 3D Zernike moments of an object

defined over image domain $\Omega_{\boldsymbol{x}} \in \mathbb{R}^3$ is as follows:

$$\lambda_{nlm} \triangleq \frac{3}{4\pi} \int_{|\boldsymbol{x}|\leq 1} I(\boldsymbol{x}) \overline{Z_{nl}^m(\boldsymbol{x})} d\boldsymbol{x}, \tag{54}$$

where $Z_{nl}^m(\boldsymbol{x})$ is the 3D Zernike function defined as

$$Z_{nl}^m(\boldsymbol{x}) = R_{nl}(r) Y_l^m(\vartheta, \psi). \tag{55}$$

Here, R_{nl} is a radial function and Y_l^m is an angular function, where $n \in [0, N_{\text{ZM}}]$ is the moments order, and $m \in [-l, l]$, $l \in [0, n]$ such that $n - |l|$ is an even number. Note that, the Equation (54) can be rewritten as a linear combination of geometric moments

$$\lambda_{nlm} = \frac{3}{4\pi} \sum_{r+s+t\leq n} \overline{\chi_{nlm}^{rst}} \hat{M}_{rst}, \tag{56}$$

where $\hat{M}_{rst}$ is the geometric moments of order $r + s + t$ that is rescaled to fit into a unit ball. The invariance to translation, rotation, and scaling is achieved by first computing the *normalized central moments* M_{rst} for $\hat{M}_{rst}$ and then taking the norms of vectors $\boldsymbol{\lambda}_{nlm} \triangleq (\lambda_{nl}^{-l}, \lambda_{nl}^{-l+1}, \cdots, \lambda_{nl}^{l})$. Here, the normalized geometrical central moments is defined as

$$M_{rst} = \int_\Omega \Big(\frac{x - \bar{x}}{R}\Big)^r \Big(\frac{y - \bar{y}}{R}\Big)^s \Big(\frac{z - \bar{z}}{R}\Big)^t H(\phi) d\boldsymbol{x}, \tag{57}$$

where

$$\begin{aligned}
R &= \sqrt{\frac{\int_\Omega \Big((x-\bar{x})^2 + (y-\bar{y})^2 + (z-\bar{z})^2\Big) H(\phi) d\boldsymbol{x}}{\int_\Omega H(\phi) d\boldsymbol{x}}} \\
K_0 &\triangleq \int_\Omega H(\phi) d\boldsymbol{x} \\
K_1 &\triangleq \bar{x} = \int_\Omega x H(\phi) d\boldsymbol{x} \\
K_2 &\triangleq \bar{y} = \int_\Omega y H(\phi) d\boldsymbol{x} \\
K_3 &\triangleq \bar{z} = \int_\Omega z H(\phi) d\boldsymbol{x}
\end{aligned} \tag{58}$$

See [62] for details.

The proposed shape prior is defined as the squared distance between an evolving shape ϕ and a reference shape in terms of the Zernike moments as follows:

$$\begin{aligned} J(\phi) &= d(\boldsymbol{\lambda}, \boldsymbol{\lambda}^{ref}) \\ &= \sum_{nlm} \|\lambda_{nlm} - \lambda_{nlm}^{ref}\|^2 \\ &= \sum_{nlm} \| \sum_{rst} \overline{\chi_{nlm}^{rst}} M_{rst} - \lambda_{nlm}^{ref}\|^2 \\ &= \sum_{nlm} \Big(\sum_{rst} \mathrm{Re}\overline{\chi_{nlm}^{rst}} M_{rst} - \mathrm{Re}\lambda_{nlm}^{ref} \Big)^2 \\ &+ \sum_{nlm} \Big(\sum_{rst} \mathrm{Im}\overline{\chi_{nlm}^{rst}} M_{rst} - \mathrm{Im}\lambda_{nlm}^{ref} \Big)^2 \end{aligned} \tag{59}$$

Note that the constant coefficient $\dfrac{3}{4\phi}$ is dropped since it does not affect the computation of the first variation of $J(\phi)$ with respect to ϕ, which is

$$\begin{aligned} \frac{\partial J(\phi)}{\partial \phi} =& 2 \sum_{nlm} \Big(\sum_{rst} \mathrm{Re}\overline{\chi_{nlm}^{rst}} M_{rst} - \mathrm{Re}\lambda_{nlm}^{ref} \Big) \Big(\sum_{rst} \mathrm{Re}\overline{\chi_{nlm}^{rst}} \frac{\partial M}{\partial \phi} \Big) + \\ & 2 \sum_{nlm} \Big(\sum_{rst} \mathrm{Im}\overline{\chi_{nlm}^{rst}} M_{rst} - \mathrm{Im}\lambda_{nlm}^{ref} \Big) \Big(\sum_{rst} \mathrm{Im}\overline{\chi_{nlm}^{rst}} \frac{\partial M}{\partial \phi} \Big) \end{aligned} . \tag{60}$$

By using the chain rule, the first variation of M_{rst} with respect to ϕ is computed as

$$\frac{\partial M_{rst}}{\partial \phi} = \sum_i \frac{\partial M}{\partial K_i} \delta_{K_i} + \delta_H, \tag{61}$$

where δ_{K_i} is the variation of K_i with respect to ϕ. See Appendix B for details. Then, the gradient descent technique is employed to minimize $J(\phi)$.

Gradient descent is employed to minimize $J(\phi)$. An example of deforming two canonical geometric shapes, i.e., a hyperbola and a sphere, to minimize the shape distance defined in Equation (59) is shown in Figure 18. Starting from those two significantly different shapes, the evolution process deforms these shapes towards a LA shape prior of order 12.

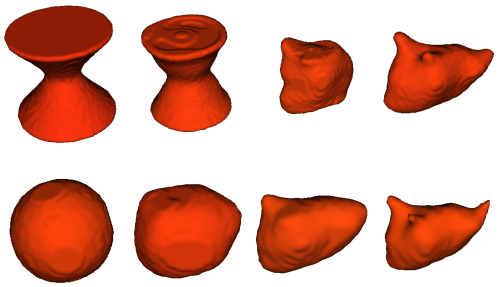

Figure 18: Deformation of hyperbola and sphere to a given LA shape. The moments order is 12.

3.1.2.3 Region Growing with a Shape Prior

Combining the region-growing energy Equation (52) with the shape prior Equation (59), the energy functional to be minimized for the LA segmentation is

$$E(\phi) = g(V_j)E_{\mathrm{RS}}(\phi) + (1 - g(V_j) - \gamma)J(\phi) + \gamma \int_{\Omega} \delta(\boldsymbol{x})|\nabla\phi(\boldsymbol{x})|d\boldsymbol{x}, \tag{62}$$

where $g(V_j)$ adjusts the weight between E_{RS} and J based on the evolving LA volume V_j. This is defined as

$$g(V_j) = \frac{1-\gamma}{1 + e^{\alpha(V_j - (\mu_V - (\beta\sigma_V)))}}, \tag{63}$$

where μ_V and σ_V are the mean and standard deviation of the LA volumes from training images, respectively, and β is associated with the radius of the seed region r^* as

$$\beta = sign(r^*)\lfloor\frac{r^* - \mu_r}{\sigma_r}\rfloor, \tag{64}$$

where μ_r and σ_r are the mean and standard deviation of the radii of the seed regions learned from training images. As can be seen from Equation (63), $g(V_j) \to 1-\gamma$ when $V_j \ll \mu_V$ and $g(V_j) \to 0$ otherwise. E_{RS} dominates the growing process initially and its role decreases as the volume of LA increases. In all of experiments, the parameters were empirically set as $\alpha = 0.03$ and $\gamma = 0.3$.

Note that $V_j = K_0$, and thus the gradient descent flow of

$$\begin{aligned}\frac{\partial E(\phi)}{\partial \phi} &= g'(K_0)\delta_{K_0}E_{\mathrm{RS}} + g(K_0)\delta(\phi(\boldsymbol{x}))p(\boldsymbol{f}(\boldsymbol{x})) \\ &\quad - g'(K_0)\delta_{K_0}J + (1 - g(K_0) - \gamma)\frac{\partial J}{\partial \phi} \\ &\quad + \gamma|\nabla\phi(\boldsymbol{x})|\nabla \cdot \Big(\frac{\nabla\phi(\boldsymbol{x})}{|\nabla\phi(\boldsymbol{x})|}\Big).\end{aligned} \tag{65}$$

The last term is the curvature at point $\boldsymbol{x}$, which smooths evolving contours. An example of the region-growing process driven by this flow is shown in Figure 19. It shows that the process explores homogeneous regions first when the robust statistic force is dominant (Figure 19 (a)-(c)) and captures fine details when the shape prior starts to play main role (Figure 19 (e)-(f)).

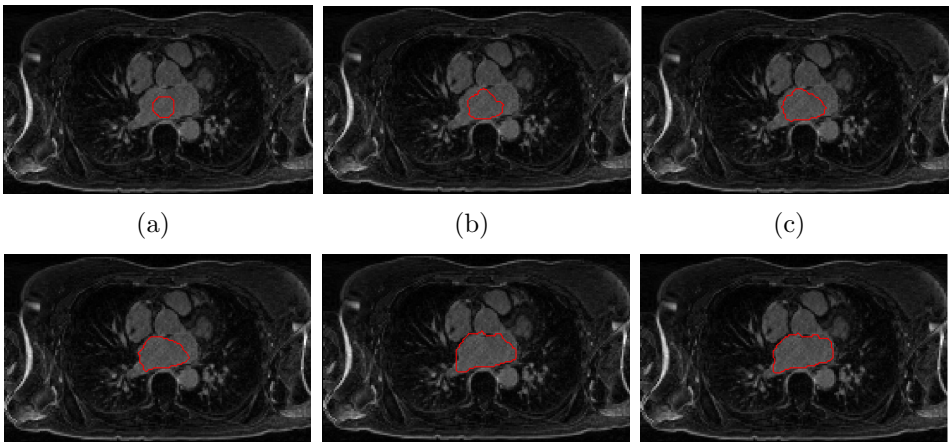

(a) (b) (c)

(d) (e) (f)

Figure 19: Region-growing process driven by robust statistics and Zernike moments shape prior.

3.1.3 Implementation

A shape prior learned from training data was used through the steps of the region-growing processing. To this end, 16 Delayed Enhanced MR images (DE-MRI) with manual segmentations were used, which include LA with wide shape variations and volume sizes.

To find the local threshold T_{local} in Equation (39), the spatial distribution of LA is determined as follows: First, the ROI of an image is set as the largest bounding box

for the non-zero elements returned by Otsu's method [64] performed on the middle slice of a training volume (see Figure 20(b)). Then, the coordinates of an LA mask is normalized to $[-1, 1] \times [-1, 1]$ by setting the origin at the center of the ROI found in the previous step. Finally, all normalized masks are summed up and normalized to lie in $[0, 1]$ as the spatial distribution of LA (see Figure 20(a)). This distribution map is rescaled to the ROI of an MRI image to be segmented, and points with probability greater than 0.5 are chosen as the mask to determine T_{local} (see Figure 20(b)). Normalizing coordinates can, to some extent, compensate the difference of volume coverages when applying the LA mask. In detecting the heart region, the ball radius was fixed as 10 mm, and the weight of curvature term in Equation (41) was 0.7 to favor a smooth final contour.

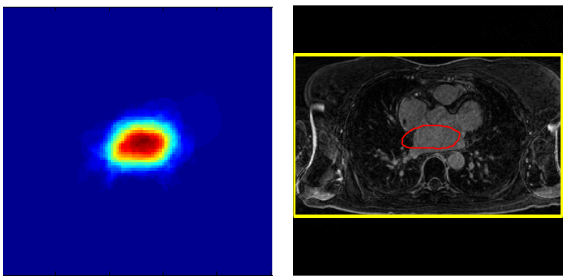

(a) (b)

Figure 20: (a) Spatial distribution of the LA in the normalized coordinate system.(b) The ROI (yellow) of an MR image and applied LA mask(red).

The Gaussian function was employed to model the distribution of the seed region radii and LA volumes from these training data. The parameters learned were $\mu_r =$ 11.6 mm, $\sigma_r = 3.1$ mm, $\mu_V = 106$ ml, and $\sigma_V = 45$ ml.

To compute the Zernike moments for the LA, each LA mask was used individually and then these moments were averaged component-wise as the shape prior. In the experiments, the moments order was set as $N_{\text{ZM}} = 12$.

Numerically, the sparse level set method [82] was utilized to realize the variational region-growing model for its efficiency. In particular, the upwind scheme was used in discretizing $|\nabla(\cdot)|$ (see [4] for details).

3.2 Experiments and Results

The proposed segmentation method was evaluated by using 64 MR images provided by Comprehensive Arrhythmia Research and Management (CARMA) Center that are publicly accessible at [12]. These data are Late-Gadolium Enhanced (LGE-MRI) from 32 patients with atrial fibrillation (AF) who have undergone radiofrequency (RF) catheter ablation for treatment of AF, of which 32 are images before RF ablation and others are after. Enhancement is hypothesized to fibrosis or endocardial tissue that is correlated with the progression of AF for the pre-ablation images, and that of post-ablation images is due mainly to the scars. Thus, these data have large variations in terms of LA shape, intensity range, and image quality. In addition, no well-defined boundaries between the LA and other heart chambers and the blood pool is not contrast enhanced.

In the experiments, all parameters were fixed as described in Section 3.1.3. The proposed method succeeded in finding the seed regions for all of the 64 images. An example of the final segmentation results is shown in Figure 21 for two LAs with significantly different shapes and volume coverages. The final segmentations capture the overall LA structure, only missing parts of the pulmonary veins (PVs).

In addition, the proposed method was compared to the standard multi-atlas-based method. Let $\{I^i_{tr}\}$ and $\{L^i_{tr}\}$, $i = 1 \cdots 16$ be a set of training and label images, respectively. The multi-atlas method works as follows: First, each training image I^i_{tr} is registered to an LGE-MRI image I_j to be segmented by searching for an optimal affine transformation T^i_{opt} using mutual information [80, 59] as a metric. Then, the corresponding label image L^i_{tr} is transformed using T^i_{opt}. Let $\tilde{T}^i_{tr}$ and $\tilde{L}^i_{tr}$ denote the transformed training and label images, respectively. Then, the non-zero region of $\tilde{L}^i_{tr}$ is selected as a ROI and refined by registering the $\tilde{T}^i_{tr}$ to I_j using the B-Spline registration method [70]. After registering all the training images to I_j, we get a

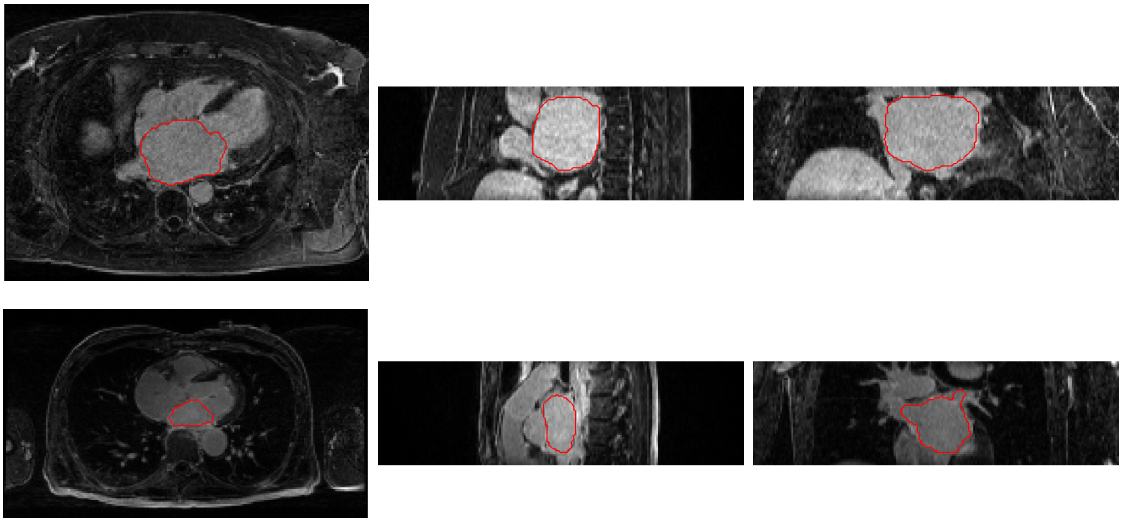

Figure 21: Segmentation of the LA with sharp shape variations and wide volume coverages. From left to right: the LA in axial, coronal, and sagittal views, respectively.

set of transformed label images associated with their registration errors from the B-Spline registration, based on which the transformed label images are fused to get a consistent probability map for the LA. This probability can be regarded as a prior for the spatial distribution of the LA in the current image I_j. On the other hand, the intensity distribution of the LA obtained by summing up the intensities within each LA label is used as the likelihood of a voxel of being the LA. Finally, the Bayesian rule is used to get the posterior probability of the LA distribution and the voxels with their probability greater than a threshold, which was 0.4 in the experiments, are chosen as the segmentation of the LA.

To quantify errors, we measure the overlap between an automatic segmentation V_a and the ground truth V_m using the standard Dice coefficient [29] and volume overlap [19]

$$\begin{aligned} Dice(V_a, V_m) &= 2\frac{|V_a \cap V_m|}{|V_a| + |V_m|} \\ Overlap(V_a, V_m) &= \frac{|V_a \cap V_m|}{|V_a \cup V_m|}, \end{aligned} \tag{66}$$

where V_a and V_m are the volumes of an image from automatic and manual segmentations. The comparison results are summarized in Table 4. In overall, the proposed

method achieves better results in terms of accuracy and the worst case. The details of this comparison is shown in Figure 22 where only the results from the patients with even ID indices are presented to save displaying space. This detailed results show that the proposed method outperformed the atlas-based method in 30 out of 32 cases in terms of the Dice measurement, and in 29 out of 32 cases in the Volume Overlap measurement.

In addition, the worst results in terms of the Dice measurement obtained using these two methods are shown in Figure 23, which illustrates the characteristics of these two types of methods. The proposed method is more flexible to the variations of the volume coverage and LA shapes because of its *localized* property, while leakage may still happen if partial boundaries are insufficient to stop the growing process, even though a shape prior is used. In addition, because of the underlying smoothness requirement in variational derivations, the proposed method has less priority to develop sharp changes over the shape, which results in the missing of some regions around the PVs. For the atlas-based method, it suffers severely from changes in the volume coverages as it is a *globalized* method. As shown in Figure 23, the existence of arms in different side of the MR images makes the final segmentation deviate away from the expected locations, even though the overall segmentations have similar shape as the ones expected.

Table 4: Comparison of segmentation accuracy between the proposed method and multi-atlas-based method

Method	Dice			Volume Overlap		
	Mean	STD	Min	Mean	STD	Min
Proposed Method	0.78	0.06	0.63	0.64	0.09	0.46
Multi-Atalas	0.69	0.11	0.27	0.54	0.13	0.15

Though it is hard to make a fair comparison between different methods because of the use of different datasets, the performance of our method seems to be competitive

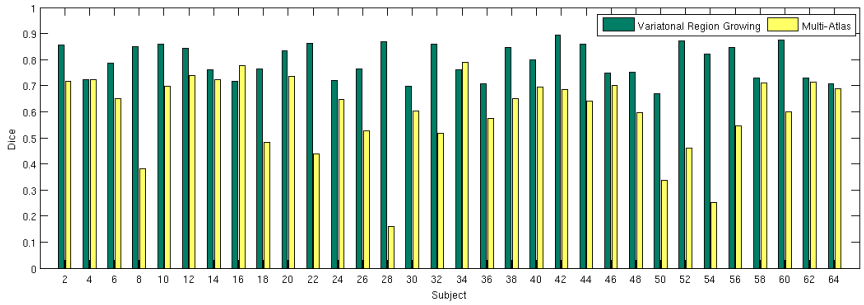

(a)

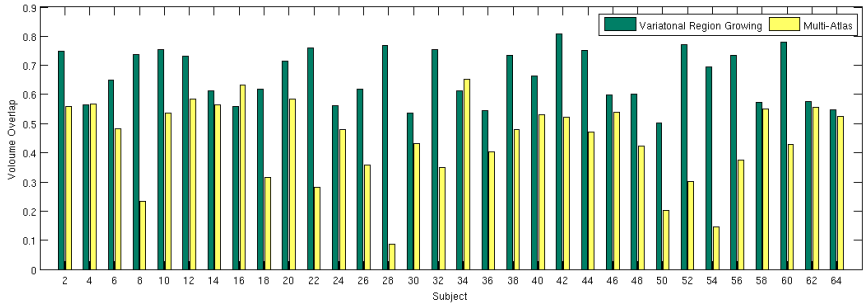

(b)

Figure 22: Comparison of segmentation accuracy in terms of Dice (a) and Volume Overlap (b) between the proposed method (green) and multi-atlas-based method (yellow).

with some of latest results. For example one state-of-the-art method [95] reports a result of 0.81 ± 0.10 with a minimum 0.47 and 0.69 ± 0.12 with a minimum of 0.30 for the Dice and Volume Overlap measures with the minimum as the worst cases, respectively. The reference method [95] achieves higher mean values since it uses a whole heart model that contains more prior knowledge while treating an MR image. However, our method has a smaller standard deviation and better performance in the worst cases because of its localized property, which focuses more on the object to be segmented.

3.3 Conclusion

An automatic segmentation scheme has been described for extracting the LA using a variational region growing with shape prior from MR data. The method starts locally from a seed region of the LA, and explores the LA region using locally computed

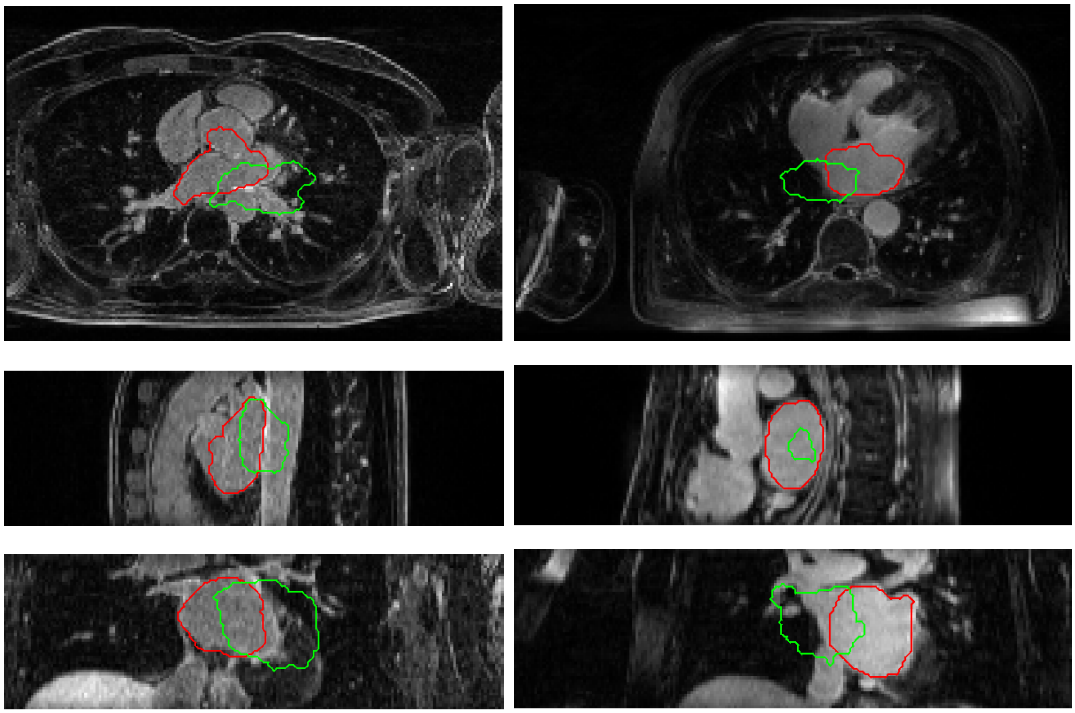

Figure 23: Comparison of the worst results (in terms of the Dice measurement) obtained by using the proposed method (first column) and atlas-based method (second column) . From top to bottom: the LA returned using the proposed method (red) and atlas-based method (green) in axial, coronal, and sagittal views, respectively.

robust statistics of the intensities and a shape prior that provides global guidance. Thus, this method is robust to shape variations and image quality. The experimental results show the ability of the proposed approach to give very reasonable results.

As indicated by our experimental results, the main problems with the segmentations occur near the PVs. Thus, in our future work, we will investigate ways to improve the segmentation accuracy by incorporating certain geometric information of the PVs with respect to the LA. In addition, we will use the segmentation results as a prior information to identify scars for MR images of post-ablations.

CHAPTER IV

APPLICATIONS OF WALL STRUCTURE SEGMENTATION

In this Chapter, applications of the LV and LA segmentations in clinical analysis are investigated. In particular, an effective computational framework is proposed to estimate the myocardial mass at risk caused by stenoses using CTA images. The LA segmentation results are utilized to identify the scar tissue resulted from post-ablation procedure in the atrial fibrillation treatment.

4.1 Estimation of Myocardial Mass at Risk

Little work has been done for estimating the myocardial mass at risk from a patient-specific heart surface segmented from CTA images, rather than using a simplified heart model such as an ellipsoid. The purpose of this study is to provide an efficient and generic computational framework for estimating the myocardial mass at risk that can capture the individual myocardial variability. Since it is straightforward to determine the mass at risk given its corresponding volume, a key step is then reduced to how to extract this volume. To this end, the relation between the myocardial mass at risk and the location of coronary artery occlusions is utilized as a basis for computations. In addition, a decomposition strategy is adopted to reduce the computational cost by first finding the regions at risk on the epicardial and endocardial surfaces, and then reconstructing the volume in between these regions as an estimate of the myocardial volume at risk.

4.1.1 Proposed Method

As shown in Figure 24, the proposed method has three major components: First, extract the coronary arteries from a CTA image and identify stenoses with severe occlusions. Second, segment the left ventricular surface from the CTA image. Third, estimate the affected mass based on the segmentations of the arteries and LV. The detail of each component is described in the following sections.

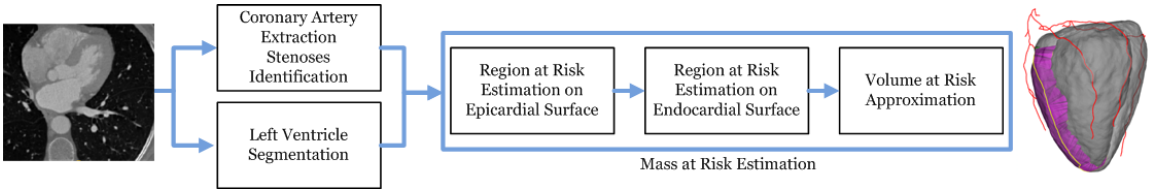

Figure 24: Flow chart of the proposed method for estimating the myocardial mass at risk.

4.1.2 Coronary Artery Extraction and Stenoses Identification

CTA images were evaluated on a Leonardo work station (Siemens, Forchheim, Germany). Coronary artery vessel analysis in terms of the degree of area and diameter stenosis was done using Syngo Circulation software (Siemens, Germany), which is a semi-automatic post-processing tool based on a region-growing algorithm. By clicking on an area in aorta just above the coronary ostia, the system delineates the coronary tree. Non-delineated segments are marked manually and then added to the dataset by the algorithm. Curved multiplanar reformations for each vessel are generated and are rotated in multiple planes to identify stenotic lesions. The degree of area stenosis is determined by using an user interface of the Circulation software. The diameter of a stenosis is identified using 3D multiplanar reformations (MPR), and the diameter is calculated by orienting a 2D MPR orthogonal to each other and then computing the measurements. In this work, arteries with luminary narrowing between 75-99% by diameter were defined as significantly stenotic and were chosen for subsequent computations. A snapshot of artery extraction and stenoses identification process is

shown in Figure 25.

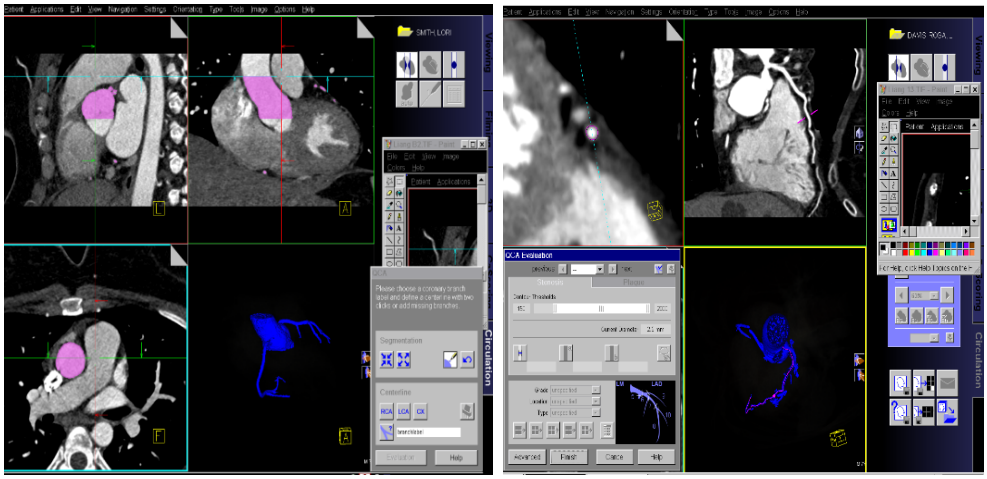

(a) (b)

Figure 25: User interface of the Syngo Circulation software for (a) segmentation of coronary arteries and (b) identification of stenosis.

4.1.3 Left Ventricle Segmentation

An automatic segmentation method [91] is applied to extract the LV. The method consists of two major steps: First, the LV is localized on the heart surface by using a shape segmentation technique; Then, the myocardial surfaces are initialized and refined by employing active contour models.

4.1.3.1 LV localization

Assume that the orientation of a CT image is given and intensity contrast exists between the blood pool and myocardium. The LV localization is determined via searching for a deep concave boundary, called a *cut contour*, on the heart surface.

4.1.3.2 Heart Surface Extraction

The heart surface is approximated by a triangulated surface of the blood poor mask. Since CT images have calibrated intensities, the blood pool mask is extracted via thresholding. A threshold of 180 in Hounsfield units was used so that the left and

right ventricles can be separated after thresholding. Then, the morphological opening operator is applied to remove noisy arteries and cut spines that may be residing in the same connected component of the heart. The largest connected component is chosen as a mask for the blood pool.

4.1.3.3 Apex Point Detection

The apex point is one salient feature that can be used to locate the LV as follows: 1) estimate the orientation of ventricles; 2) search for the LV apex which is the *left* tip point with respect to the estimated orientation. Specifically, the orientation of the heart surface is estimated by searching for the principal component of the high curvature points on the heart surface. As shown in Figure 26(a), the estimated orientation **H** shows the direction of ventricles, based on which a plane L_O is determined to define the directions of left and right. Then, these high curvature points are picked in order to label the heart surface according to their projections in the direction **H**. Ideally, two labeled regions will be found as shown in the figure. The one with a larger centroid in direction **N** is selected as the region that contains the apex point. Finally, the apex point is approximated by a point in this region that has the largest projection in the direction **H**.

4.1.3.4 LV Surface Segmentation

The segmentation of the LV surface begins by computing the distance field starting from the apex point. As has been shown in [91], the distribution of the total length of isocontours on this distance field can be modeled by a bi-mode function, where the first mode represents the distribution by a polynomial as the isocontour travels on the LV and the second one uses a Gaussian function to capture this relation when the isocontour propagates further away. A turning point of these two modes indicates the location of a cut contour that separates the LV from the other structures (see Figure 26(b)). The optimal turning point is determined by minimizing the least-squares

fitting error in estimating the model parameters. The geometric active contour model [48, 13] is employed on the heart surface to refine the initial contour C_0. As can be seen from Figures 26(b) and 26(c), starting from a location away from the real *cut contour*, the contour C_0 converges to the desired location, which identities the LV endocardial surface.

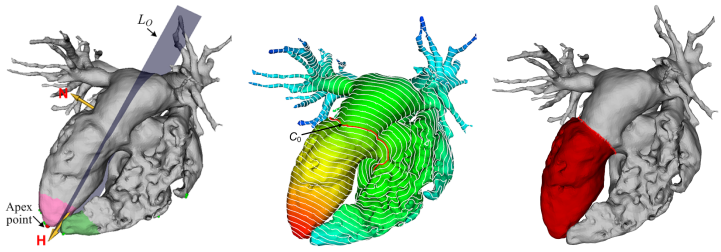

(a) (b) (c)

Figure 26: The LV localization process. (a) Apex point detection.The plane L_O with normal **N** identifies the direction of *left* and *right*. The apex point lies on the labeled region (pink) that mainly resides above plane L_0. (b) Initialized cut contour C_0. (c) Localized LV on the heart surface.

4.1.3.5 Myocardial Wall Segmentation

The endocardial surface indicates the LV location, which is rasterized to get its 3D mask for refinement. The epicardial mask is initialized by utilizing a variational region-growing model [33] that takes an outward neighborhood of the endocardium as a seed region. After that, a localized region-based active contour model [52] is applied with a shape constraint imposed by these initial masks to refine the myocardial segmentation. Finally, the voxels reside in the blood pool are removed to get a complete wall. An example of the wall segmentation process is shown in Figure 27.

4.1.4 Volume at Risk Estimation

Given the segmentations of coronary arteries and myocardial wall, and identified severe stenoses, the mass at risk caused by these stenoses can be estimated by using an efficient computational method [93] as follows: First, determine the region affected

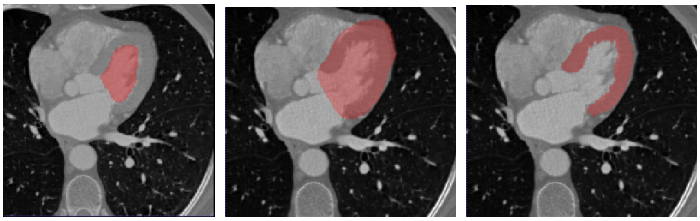

(a) (b) (c)

Figure 27: Myocaridal wall segmentation. (a) Initial endocardial mask. (b) Initial epicardial mask. (c) Myocardial wall after refinement.

by the stenoses on the epicardial surface. Next, extract the corresponding region at risk on the endocardial surface. Finally, combine these two regions to get the volume at risk and estimate its corresponding mass. The main steps are described in the following sections. See [93] for more details.

4.1.4.1 Determination of Region at Risk on the Epicardial Surface

Since the extracted coronary centerlines do not lie exactly on the epicardial surface, the centerline points are projected onto the epicardial surface. Then, an efficient computational method [75, 9] is applied to reconstruct the geodesic distance field on the epicardial surface using the projected arteries as source curves, which define the zero level set of the distance field. The key observations used in this method are that adjacent triangles can be virtually unfolded to a common plane, and the geodesic distance inside a triangle of a triangulated surface is a straight line. Thus, the distance field is propagated along straight lines through the so-called *windows* of each triangle edge. There are two types of curve sources, *i.e.*, point source and line source, that induce a set of windows on the edge of a triangle as shown in Figure 28. One advantage of this window-based formulation is that all computations can be done in the local coordinates defined by triangle $\triangle p_0 p_1 p_2$. Each window is described by a seven dimensional vector $(type, id, b_0, b_1, d_0, d_1, dir)$, where $type$ is either point or line source, id is the index of the source, b_0 and b_1 specify the endpoints of a window, d_0 and d_1 are the distances from a window endpoints to their closest source S, and

dir shows from which side of x-axis that the source S propagates. Starting from the source curves, the distance information is propagated through adjacent triangles in a Dijkstra-like manner (see [75, 9] for details). A list of windows is maintained for each edge of a triangle to record the geodesic distance information for points inside each window. After the distance field is computed over all triangles, each point on a triangle edge is associated with its closest point on the source curves, *i.e.*, coronary arteries. Then, the region at risk caused by a stenosis is approximated by the region in which all of its inner points are associated with the affected artery points.

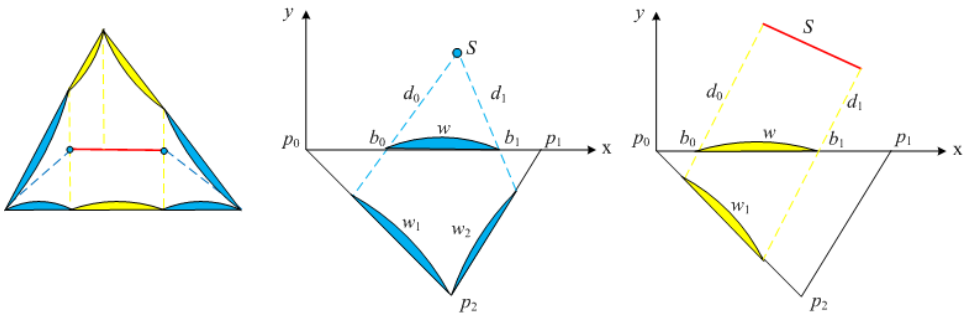

Figure 28: Distance field computation on a triangulated surface. Left: Windows induced by point sources (blue) and line source (yellow); Middle: Window propagation induced by a point source; Right: Window propagation induced by a line source.

4.1.4.2 Estimate of Volume at Risk

Let M_{epi} be the region at risk on the epicardial surface. Correspondingly, the region at risk on the endocarial surface can be approximated by the projection of M_{epi}. Then, the volume at risk is approximated by the volume defined in between those two regions. In order to reduce computational cost, an efficient method is employed to find the volume at risk as follows: (a) extract the outer contour of the region M_{epi}; (b) determine the region at risk on the endocardial surface, denoted by M_{endo}; (c) construct the volume in between these two regions.

Specifically, in step (a), the contour extraction is formulated as a distance propagation problem. To this end, all points that have equal geodesic distance to both

affected and unaffected artery points are selected as *potential boundary points*. In addition, any potential boundary points are considered as neighbors if they lie on adjacent triangles. Then, choosing a boundary point, *e.g.*, a stenosis point, we can take one of its neighboring points each time as the second point to propagate the distance field among all of the un-visited potential boundary points by using the Dijkstras algorithm [24]. Each time, one shortest path is obtained via backtracking the distance field from the farthest point to the starting point. Finally, the longest shortest path is chosen as the contour for the region at risk. A simulated example is given in Figure 29. There are three simulated segments, one of which is affected by a stenosis, denoted by S_0 . Here, n_1 and n_2 are the neighbors of S_0. In this case, two shortest paths, either starting from direction $\overrightarrow{S_0 n_1}$ or $\overrightarrow{S_0 n_2}$, were found by the method and the longest one was selected as the final result.

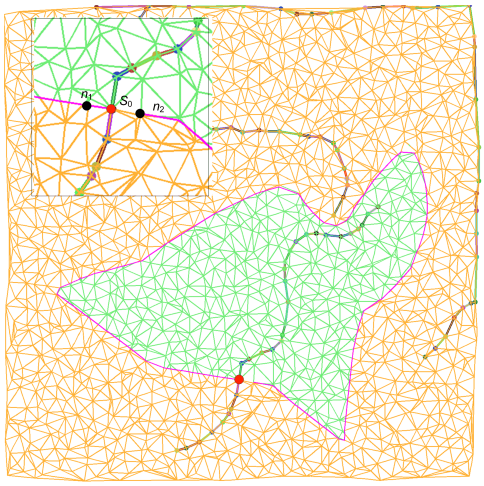

Figure 29: An example of contour extraction with simulated segments. The points are labeled based the property of their closest artery points either as unaffected (yellow) or affected (green). S_0 is the starting point, n_1 and n_2 are its two neighbors.

In step (b), each of the contour point is projected onto the endocardial surface by finding its closest point on the surface. If the projections of two adjacent points do not share a common triangle, interpolation is used to connect these two projected points by searching for the shortest path between these two points using the Dijkstra's

algorithm [24]. The classical flood fill algorithm is used to fill in the region within the projected contour, which has the same the direction as the original contour.

Finally, the two regions at risk are linked by triangulating the space between the original and projected contours to form a closed volume as an approximation of the myocardial volume at risk. The triangle vertices of the risk volume are ordered so that the normals of all triangles are consistent with each other. The value of this volume is computed as [23, 86]

$$V = \frac{1}{6} \sum_{k=1}^{F} g_k \cdot \mathbf{N}_k, \tag{67}$$

where F is the number of triangles, $g_k = (x_1^k + x_2^k + x_3^k)/3$ and $\mathbf{N}_k = \overrightarrow{x_1^k x_2^k} \bigwedge \overrightarrow{x_1^k x_3^k}$ for the kth triangle with its three vertices as x_1^k, x_2^k, and x_3^k. The overall volume estimation process is illustrated by Figure 30.

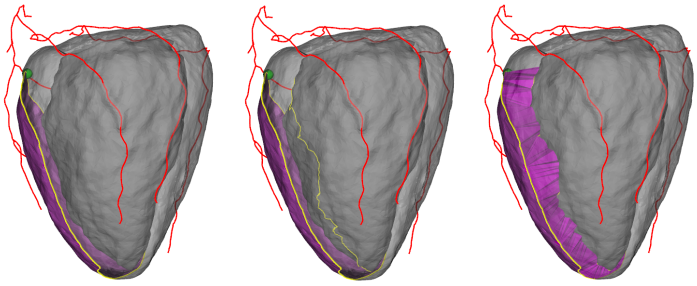

(a) (b) (c)

Figure 30: Volume at risk estimation process. (a) Extract the area at risk (purple) on the epicardial surface given the stenosis location (greed dot) on the coronary centerlines (red lines). (b) Trace out the risk contour (yellow) on the endocardial surface. (c) Construct the volume at risk (purple).

4.1.5 Experimental Results

In implementation of the LV segmentation method described in Section 4.1.3, an open source package ITK [34] was used for basic image processing tasks such as morphological and logic operations, conversion between triangle mesh and image volume. The convex hull extraction and 3D visualization were realized using VTK [81].

This study was approved by the Institutional Review Board. 11 human cardiac CTA images were used to validate the proposed computational framework. The dataset includes anomaly cases (hypertrophic cardiomyopathy where the myocardium is hypertrophied) and volumes with different scanning quality.

4.1.5.1 Distance Computation on Surfaces

Distance computation is a key component in the overall process, which is used to find the shortest path between two points on a surface. A comparison of the shortest path obtained by using four popular methods is shown in Figure 31. In this example, both 2D and 3D meshes were used to illustrate the performance of these methods. It is clear that the extract geodesics method [75, 9] returns the best result, and the Dijkstra's algorithm the worst.

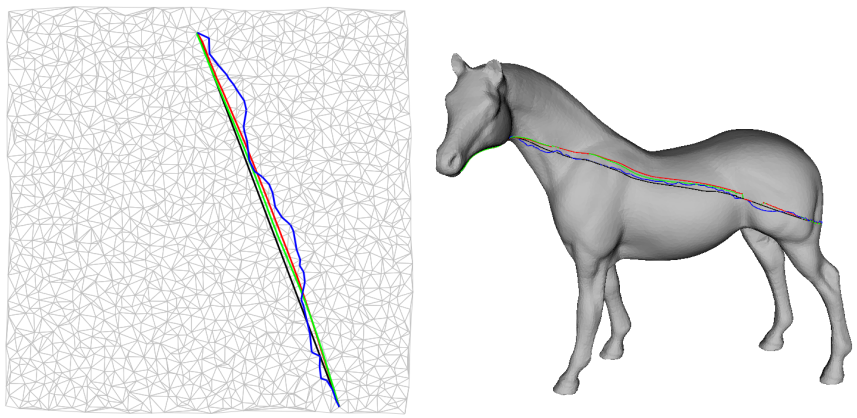

(a) (b)

Figure 31: Comparison of four distance computation methods: Dijkstra(blue), Fast Marching (red), Fast Sweeping (green), and Exact Geodesics (black). (a) Minimal paths on a 2D triangle mesh. (b) Minimal paths on a 3D triangle mesh.

To quantitatively evaluate the accuracy of the exact geodesics method, 2D triangle mesh was used for its simplicity in computing the real distance function $g(\cdot)$ between two given points. In this experiment, triangles with different sizes were generated randomly from a fixed 2D domain. Specifically, 10 triangle meshes were generated for each given number of vertices. The source polylines were created with random

shapes. Errors were measured by using the maximal absolute difference between $g(\cdot)$ and the distance $D(\cdot)$ returned by the algorithm, and the maximal and average relative differences defined by $|D(\cdot) - g(\cdot)|/g(\cdot)$ between the distances as in [75]. The errors of the algorithm are given in Table 5, which further validate the accuracy of the algorithm.

Table 5: Distance computation errors at different mesh resolutions

number of vertices	maximum absolute	maximum relative	avreage relative
100	0.1791	0.0147	2e-4
400	0.0657	0.0043	1.34e-5
1600	0.0304	0.0015	1.19e-6
3600	0.0063	0.0001	1.36e-7
6400	0.0143	0.0004	2.2e-7
10000	0.0227	0.0004	3.5e-7

Therefore, the exact geodesic distance method was adopted in the proposed computational framework.

4.1.5.2 Validation

For validation, the percentages of the myocardial mass at risk estimated from CTA images by using the proposed method were compared to their corresponding values determined from SPECT MPI. The myocardial mass was computed by assuming a uniform density of the myocardium as 1.05g/mL. Since the CTA analysis was done blindly to the SPECT results, the normal cases were used in the correlation analysis to account for the false-positive or positive-false reports that may happen in either of these two measurements. The anatomic mass at risk estimated from CTA images for these 11 patients was correlated with the physiological mass at risk computed from SPECT. The results are shown in Figure 32. The relationship between the two measurements are $y = 0.69x + 4.85\%$ and $r = 0.89$. In addition, Bland-Altman analysis [8] was performed to study the agreement between the mass at risk estimated

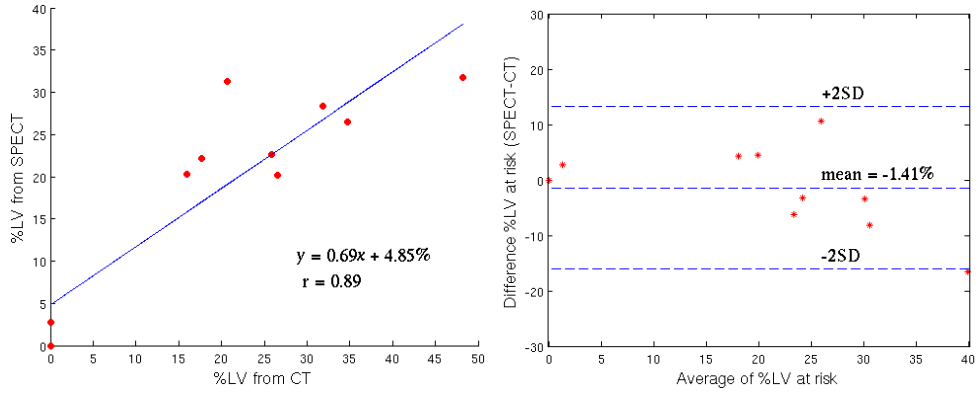

(a) (b)

Figure 32: (a) Correlation analysis. (b) Bland-Altman plot for %LV of CTA vs. SPECT.

from CTA and SPECT images. The proposed method achieved good agreement with a mean difference of -1.4% (STD = 7.4%).

4.2 Scar Tissue Segmentation in DE-MRI

4.2.1 Proposed Method

To segment the scar tissue from DE-MRI images, an effective method is proposed that utilizes the geometric and intensity information of the left atrial wall. The key observation is that the scar tissue lies around a thin layer outside the LA chamber and has higher intensity values than the surrounding tissues (see Figure 33). In order

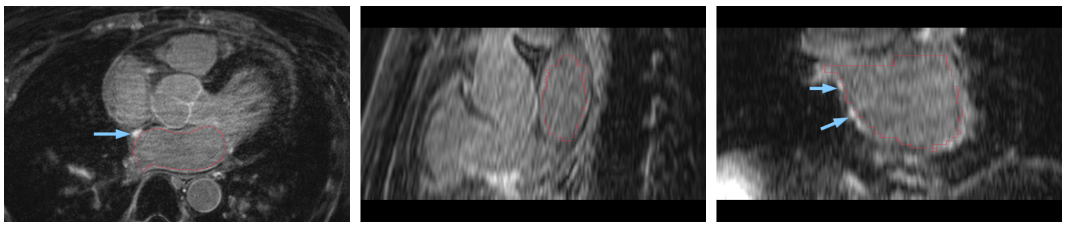

(a) (b) (c)

Figure 33: Scar tissue in a DE-MRI image. The LA is highlighted with red contour. From left to right: the scar tissue in axial, sagittal, and coronal views, respectively.

to identify the scar tissue from a DE-MRI image, the wall region of the LA is first segmented. Then, the extraction of the scar is restricted in the wall region.

4.2.2 Left Atrial Wall Segmentation

Denote the training DE-MR images as $I_i : i = 1, \ldots, n$ where $I_i : \mathbb{R}^3 \to \mathbb{R}$ and the corresponding segmentation of the endocardium as binary images $J_i : \mathbb{R}^3 \to \{0, 1\}$.

Note that the wall is a thin layer around 3 mm away from the endocardium. Thus, the corresponding epicardium is initially represented by $\bar{J}_i : \mathbb{R}^3 \to \{0, 1\}$, which is constructed by expanding J_i outward for 3 mm. To utilize both the shape information and intensity characteristics of the wall, an active contour scheme is designed for its segmentation. Let $S_i \subset \mathbb{R}^3$ be a surface and $\phi : I_i \to \mathbb{R}$ the signed distance function such that $\phi > 0$ represents the inside of S_i and $\phi < 0$ otherwise. Similarly, denote the absolute distance function of $\bar{J}_i$ as $\tilde{\phi}$. Then, the energy functional to be minimized is defined as

$$\begin{aligned} E(\phi) =& \lambda \int_{I_i} \delta(\phi(\boldsymbol{x})) \int_{I_i} B(\boldsymbol{x}, \boldsymbol{y}) F(I(\boldsymbol{y}), \phi(\boldsymbol{y})) d\boldsymbol{y} d\boldsymbol{x} \\ &+ (1 - \lambda) \int_{\bar{J}_i} \tilde{g}(\tilde{\phi}(\boldsymbol{x})) \delta(\boldsymbol{x}) |\nabla \phi(\boldsymbol{x})| d\boldsymbol{x} \end{aligned}, \tag{68}$$

where $B(\boldsymbol{x}, \boldsymbol{y})$ is a characteristic function of radius r for any $\boldsymbol{x}, \boldsymbol{y} \in I_i$, and $\tilde{g} : \mathbb{R} \to \mathbb{R}^+$ is a feature function that imposes a shape constraint,

$$\tilde{g}(\tilde{\phi}) = (d_{max} - d_{min}) \Big(1 + exp\Big(\frac{-\tilde{\phi} - \beta}{\alpha}\Big)\Big)^{-1} + d_{min}. \tag{69}$$

The parameters d_{max}, d_{min}, α and β control the range of this constraint over $\bar{J}_i$, which were empirically set as $\alpha = 1$, $\beta = 5$, $d_{max} = 1.0$ mm and $d_{min} = 0.02$ mm. The term $F(I(\boldsymbol{y}), \phi(\boldsymbol{y}))$ is a a localized Chan-Vese energy [14, 52]. The first term attracts the contour towards edges while the second term imposes a constraint so that the evolution is only allowed around a small neighborhood of the expanded LA wall $\bar{J}_i$.

The gradient descent flow of $E(\phi)$ is

$$\begin{aligned} \frac{\partial \phi(\boldsymbol{x})}{\partial t} =& \lambda \delta(\phi(\boldsymbol{x})) \int_{I_i} B(\boldsymbol{x}, \boldsymbol{y}) \delta(\phi(\boldsymbol{y})) \cdot (-(I(\boldsymbol{y}) - u_{\boldsymbol{x}})^2 + (I(\boldsymbol{y}) - v_{\boldsymbol{x}})^2) d\boldsymbol{y} \\ &+ (1 - \lambda) \Big(\tilde{g} |\nabla \phi| \kappa + \xi \tilde{g} |\nabla \phi| \ + \nabla \tilde{g} \cdot \nabla \phi \Big)(\boldsymbol{x}) \end{aligned}. \tag{70}$$

where κ is the curvature of the contour at $\boldsymbol{x}$. Numerically, the sparse level set method [82] was used to realize the variational region-growing model for its efficiency. In particular, the upwind scheme was used in discretizing $|\nabla(\cdot)|$ (see [4] for details).

4.2.3 Scar Tissue Segmentation

Observe from the image that scar regions are usually brighter than normal tissues. Therefore, for each subject, the intensity inside the wall is modeled as a two-mode function, represented by a mixture of two Gaussians. In addition, to reduce the effect of mis-segmented wall voxels, the wall is re-sampled by using the intensity distribution of the LA as a prior.

Let $h(x) = 1.0 - \gamma q(x)$ be the dissimilarity of intensity x belonging to the LA, where $W_i : \mathbb{R}^3 \to \{0, 1\}$ is a mask of the segmented wall, and $q(x)$ is the normalized frequency of the intensity x. Denote the intensity histogram of the wall as $n : \mathbb{R} \to \mathbb{R}^+$. Then, the histogram is re-sampled as $\tilde{n}(x) = n(x)h(x)$. Thus, a sequence of intensities is constructed by iteratively inserting $\tilde{n}(x)$ number of x into the array, which is denoted by $\mathbf{y} = (y_1, y_2, \cdots, y_w)$. The parameters of the Gaussian mixture model are estimated by using the Expectation Maximization (EM) algorithm [21]. Specifically, the probability density function of the mixture distribution is

$$p(y_i|\boldsymbol{\theta}) = \sum_{j=1}^{2} \alpha_j f(y_i; \mu_j, \sigma_j), \tag{71}$$

where $\boldsymbol{\theta} = (\alpha_1, \alpha_2, \mu_1, \mu_2, \sigma_1, \sigma_2)$ is unknown parameters of the mixture model. There does not exist a closed-form solution for optimizing the Equation (71) given the observed data $\mathbf{y}$. In stead, the EM algorithm is utilized to iteratively solve the problem in two steps as follows:

1. E-step: Compute an auxiliary function

$$\begin{aligned} Q(\boldsymbol{\theta}, \boldsymbol{\theta}^{(t)}) &= E[\log p(\mathbf{y}, \mathbf{z}|\boldsymbol{\theta})|\mathbf{y}, \boldsymbol{\theta}^{(t)}] \\ &= \sum_{i=1}^{w} \sum_{j=1}^{2} E[z_i = j|\mathbf{y}, \boldsymbol{\theta}^{(t)}] \alpha_j f(y_i; \mu_j, \sigma_j), \end{aligned} \tag{72}$$

which in turn maximizes original likelihood function. Here, $\mathbf{z} = (z_1, z_2, \cdots, z_w)$ is an indicator function that shows from which component the observation was generated, and $\boldsymbol{\theta}^{(t)}$ is the model parameters at the tth iteration. The expectation of $[z_i = j|y_i, \boldsymbol{\theta}^{(t)}]$ can be determined by using the Bayes' rule as

$$\begin{aligned} E[z_i = j|y_i, \boldsymbol{\theta}^{(t)})] &= \frac{p(z_i = j|\boldsymbol{\theta}^{(t)}))p(y_i|z_i = j, \boldsymbol{\theta}^{(t)}))}{p(y_i|\boldsymbol{\theta}^{(t)})} \\ &= \frac{\alpha_j^{(t)} f(y_i; \mu_j^{(t)}, \sigma_j^{(t)})}{\sum_{k=1}^{2} \alpha_k^{(t)} f(y_i; \mu_k^{(t)}, \sigma_k^{(t)})}. \end{aligned} \tag{73}$$

2. M-step: Update $\boldsymbol{\theta}$ by solving

$$\boldsymbol{\theta}^{(t+1)} = \arg\max_{\boldsymbol{\theta}} Q(\boldsymbol{\theta}, \boldsymbol{\theta}^{(t)}). \tag{74}$$

This is a standard Maximum Likelihood Estimation (MLE) problem, and the optimal value of each parameter is determined by setting the derivative of $Q(\boldsymbol{\theta}, \boldsymbol{\theta}^{(t)})$ with respect to the corresponding parameter to zero. Explicitly, the estimate of $\boldsymbol{\theta}$ is

$$\alpha_j^{(t+1)} = \frac{1}{w} \sum_{i=1}^{w} E[z_i = j|y_i, \boldsymbol{\theta}^{(t)})], \tag{75}$$

$$\mu_j^{(t+1)} = \frac{\sum_{i=1}^{w} E[z_i = j|y_i, \boldsymbol{\theta}^{(t)})] y_i}{\sum_{i=1}^{w} E[z_i = j|y_i, \boldsymbol{\theta}^{(t)})]}, \tag{76}$$

$$\sigma_j^{(t+1)} = \sqrt{\frac{\sum_{i=1}^{w} E[z_i = j|y_i, \boldsymbol{\theta}^{(t)})](y_i - \mu_j^{(t+1)})^2}{\sum_{i=1}^{w} E[z_i = j|y_i, \boldsymbol{\theta}^{(t)})]}}. \tag{77}$$

Iterate these two steps until the difference between parameter updates is small than a threshold.

Finally, the component associated with a larger mean intensity is chosen as a distribution of the scar region. The voxels with intensity values greater than a threshold determined from the distribution are classified as elements of the scar region. Typically, this threshold is set as the mean value of the scar distribution.

4.2.4 Experimental Results

To test the proposed method, 16 cardiac DE-MRI images were used in segmentation. These were post-ablation images taken at either 1, 3, or 6 months following ablation.

In wall segmentation, the weight was set as $\lambda = 0.5$, and the ball size was $r = 1.0$ mm. The proposed method succeeded in extracting all of the LA walls. One example of segmented wall is shown in Figure 34. Note that mis-segmentation exists due to poor boundaries along heart septum and the use of a simplified assumption that the wall has a uniform thickness. This observation is reflected in Figure 35(a) where the LA-like voxels dominant the histogram of the LA voxels. After resampling the wall histogram, a well-defined two-mode distribution is achieved, which is approximated by a mixture of Gaussian model (see Figure 35(b)). In experiments, $\gamma = 0.9$ was used to weight the prior information from LA intensity distribution. The identified scar tissue with and without using the LA prior was compared as shown in Figure 36. It is clear that mis-segmentation has been significantly reduced by using the LA prior.

In the future work, other prior knowledge about the distribution of LA scars will be integrated. For example, research shows the scars tend to reside around the pulmonary veins. In addition, quantitative validation will be performed on the segmentation results against manual segmentations conducted by radiologists.

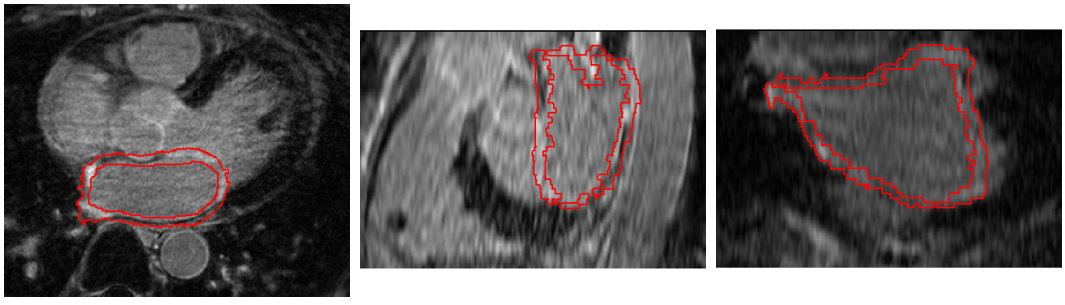

(a) (b) (c)

Figure 34: Extracted LA wall. From left to right: the LA wall in axial, sagittal, and coronal views, respectively.

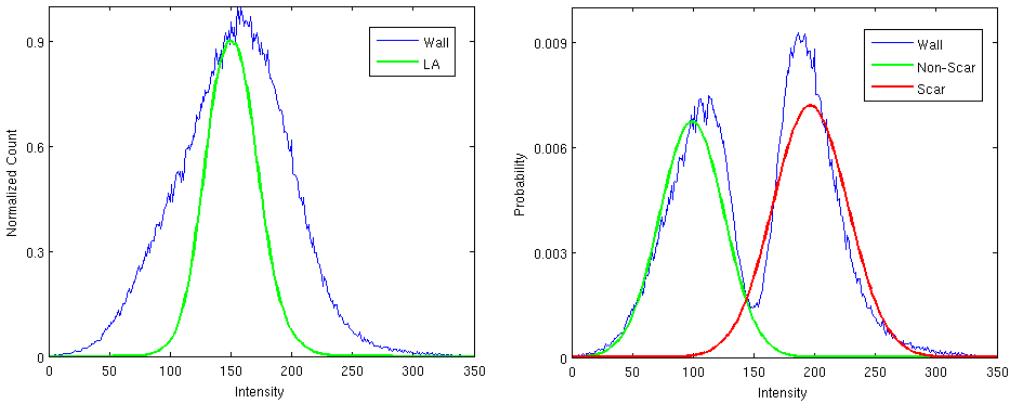

(a) (b)

Figure 35: (a) Normalized histogram for the LA (green) and wall (blue) intensities. (b) Resampled intensity distribution of the wall (blue) and estimated mixture distribution for non-scar (green) and scar (red) regions.

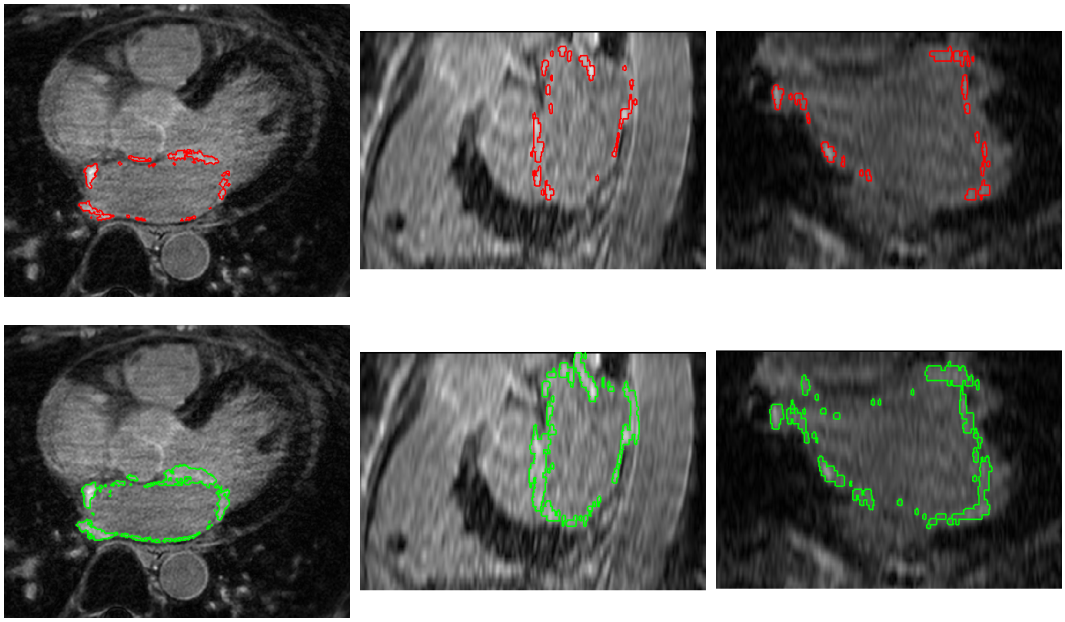

Figure 36: Comparison of scar segmentation with (first row) and without (second row) using LA intensity as a prior. From left to right: the identified scars in axial, sagittal, and coronal views, respectively.

APPENDIX A

DIFFERENTIAL GEOMETRY OF SURFACES

Given the definition in (25), the discretized gradient operator on T_k is computed as [50]

$$\begin{aligned}\nabla_{T_k} f(p_1) &= \sum_{i,j=1}^{2} g^{ij} \frac{\partial f}{\partial \chi^j} \partial_{\chi^i} \\ &= (f(p_1) - f(p_3), f(p_2) - f(p_3)) g^{-1} \begin{pmatrix} \partial_{\chi^1} \\ \partial_{\chi^2} \end{pmatrix}, \\ &= (f(p_1) - f(p_3), f(p_2) - f(p_3)) \\ &\times \begin{pmatrix} \partial_{\chi^1} \cdot \partial_{\chi^1} & \partial_{\chi^1} \cdot \partial_{\chi^2} \\ \partial_{\chi^2} \cdot \partial_{\chi^1} & \partial_{\chi^2} \cdot \partial_{\chi^2} \end{pmatrix}^{-1} \begin{pmatrix} p_1 - p_3 \\ p_2 - p_3 \end{pmatrix}\end{aligned} \tag{78}$$

where $\partial_{\chi^1} = p_1 - p_3$ and $\partial_{\chi^2} = p_2 - p_3$ are the two tangent vectors at p_3 that span the tangent plane T_pM of a surface M. The matrix $g^{-1} = (g^{i,j})$ is the inverse of the Riemannian metrics on M with

$$g = (g_{i,j}) = \begin{pmatrix} \partial_{\chi^1} \cdot \partial_{\chi^1} & \partial_{\chi^1} \cdot \partial_{\chi^2} \\ \partial_{\chi^2} \cdot \partial_{\chi^1} & \partial_{\chi^2} \cdot \partial_{\chi^2} \end{pmatrix}. \tag{79}$$

The vector field on T_k can be represented in the local coordinate as $\mathbf{V} = v_1\partial_{\chi^1} + v_2\partial_{\chi^2}$. The discretization of the divergence operator on T_k is

$$
\begin{aligned}
&\nabla_{T_k} \cdot \mathbf{V}(p_1) \\
&= \frac{1}{\sqrt{G}} \sum_{i=1}^{2} \frac{\partial}{\partial \chi^i}(\sqrt{G} v^i) \\
&= \frac{\partial}{\partial \chi^1}(v_1) + \frac{\partial}{\partial \chi^2}(v_2) \\
&= \Big(g^{11}(\mathbf{V}(p_1) - \mathbf{V}(p_3)) + g^{21}(\mathbf{V}(p_2) - \mathbf{V}(p_3)) \Big) \partial_{\chi^1} \\
&+ \Big(g^{12}(\mathbf{V}(p_1) - \mathbf{V}(p_3)) + g^{22}(\mathbf{V}(p_2) - \mathbf{V}(p_3)) \Big) \partial_{\chi^2}.
\end{aligned}
\tag{80}
$$

APPENDIX B

CALCULUS OF VARIATIONS OF GEOMETRIC MOMENTS

The gradient of the normalized geometric moments M_{rst} of order $N_{GM} = r + s + t$ with respect to ϕ is computed as follows,

$$\begin{aligned}\frac{\partial M_{rst}}{\partial K_0} = &\frac{rK_1}{RK_0^2}\eta_{r-1,s,t} + \frac{sK_2}{RK_0^2}\eta_{r,s-1,t} + \frac{tK_3}{RK_0^2}\eta_{r,s,t-1} \\ &+ \Big(\frac{K_1\eta_{1,0,0} + K_2\eta_{0,1,0} + K_3\eta_{0,0,1}}{R^2K_0^3} \\ &- \frac{\eta_{2,0,0} + \eta_{0,2,0} + \eta_{0,0,2}}{2R^2K_0^2}\Big)\eta_{r,s,t}\end{aligned} \tag{81}$$

$$\frac{\partial M_{rst}}{\partial K_1} = -\frac{r(R^2K_0^2 + K_1\eta_{1,0,0})}{R^3K_0^3}\eta_{r-1,s,t} \tag{82}$$

$$\frac{\partial M_{rst}}{\partial K_2} = -\frac{s(R^2K_0^2 + K_2\eta_{1,0,0})}{R^3K_0^3}\eta_{r,s-1,t} \tag{83}$$

$$\frac{\partial M_{rst}}{\partial K_3} = -\frac{t(R^2K_0^2 + K_3\eta 1,0,0)}{R^3K_0^3}\eta_{r,s,t-1} \tag{84}$$

$$\frac{\partial K_0}{\partial \phi} = \delta, \frac{\partial K_1}{\partial \phi} = x\delta, \frac{\partial K_2}{\partial \phi} = y\delta, \frac{\partial K_3}{\partial \phi} = z\delta, \tag{85}$$

where δ is the Dirac function. Thus the terms in Equation (61) are computed as follows:

$$\begin{aligned}\frac{\partial M_{rst}}{\partial K_0}\delta_{K_0} = &\Big(\frac{rK_1}{RK_0^2}\eta_{r-1,s,t} + \frac{sK_2}{RK_0^2}\eta_{r,s-1,t} + \frac{tK_3}{RK_0^2}\eta_{r,s,t-1} \\ &+ \Big(\frac{K_1\eta_{1,0,0} + K_2\eta_{0,1,0} + K_3\eta_{0,0,1}}{R^2K_0^3} \\ &- \frac{\eta_{2,0,0} + \eta_{0,2,0} + \eta_{0,0,2}}{2R^2K_0^2}\Big)\eta_{r,s,t}\Big)\delta\end{aligned} \tag{86}$$

$$\frac{\partial M_{rst}}{\partial K_1}\delta_{K_1} = -\Big(\frac{r(R^2K_0^2 + K_1\eta - 1, 0, 0)}{R^3K_0^3}\eta_{r-1,s,t}\Big)x\delta \tag{87}$$

$$\frac{\partial M_{rst}}{\partial K_2}\delta_{K_2} = -\Big(\frac{r(R^2K_0^2 + K_1\eta_{1,0,0})}{R^3K_0^3}\eta_{r-1,s,t}\Big)y\delta \tag{88}$$

$$\frac{\partial M_{rst}}{\partial K_3}\delta_{K_3} = -\Big(\frac{t(R^2K_0^2 + K_3\eta 1, 0, 0)}{R^3K_0^3}\eta_{r,s,t-1}\Big)z\delta \tag{89}$$

$$\delta_H = \Big(\frac{x - \bar{x}}{R}\Big)^r\Big(\frac{y - \bar{y}}{R}\Big)^s\Big(\frac{z - \bar{z}}{R}\Big)^t\delta \tag{90}$$

REFERENCES

[1] Appia, V., Ganapathy, B., Abufadel, A., Yezzi, A., and Faber, T., "A regions of confidence based approach to enhance segmentation with shape priors," in *Proceedings of SPIE Medical Imaging*, p. 753302, 2010.

[2] Appia, V., Ganapathy, B., Yezzi, A., and Faber, T., "Localized principal component analysis based curve evolution: A divide and conquer approach," *Computer Vision, IEEE International Conference on*, pp. 1981–1986, 2011.

[3] Attene, M., Katz, S., Mortara, M., Patanè, G., Spagnuolo, M., and Tal, A., "Mesh segmentation - a comparative study," in *Proceedings of the IEEE International Conference on Shape Modeling and Applications*, pp. 14–25, 2006.

[4] Aubert, G. and Kornprobst, P., *Mathematical Problems in Image Processing: Partial Differential Equations and the Calculus of Variations (Applied Mathematical Sciences)*. Secaucus, NJ, USA: Springer-Verlag New York, Inc., 2006.

[5] Bajaj, C., Goswami, S., Yu, Z., Zhang, Y., Bazilevs, Y., and Hughes, T., "Patient specific heart models from high resolution ct," in *International Symposium on Computational Modeling of Objects Represented in Images: Fundamentals, Methods,and Applications*, 2006.

[6] Ballard, D., "Generalizing the hough transform to detect arbitrary shapes," *Pattern Recognition*, vol. 13, no. 2, pp. 111–122, 1981.

[7] Beliveau, P., Setser, R., Cheriet, F., White, R., and O'Donnelle, T., "Computation of coronary perfusion territories from ct angiography," in *34th Annual Computers in Cardiology Conference*, pp. 34:753–756, September 2007.

[8] Bland, J. and Altman, D., "Statistical methods for assessing agreement between two methods of clinical measurement," *Lancet*, vol. 1, no. 8476, 1986.

[9] Bommes, D. and Kobbelt, L., "Accurate computation of geodesic distance fields for polygonal curves on triangle meshes," in *Proceedings of the Vision, Modeling, and Visualization Conference*, pp. 151–160, 2007.

[10] Calvin, M., Qi, R., and Raghavan, V., "A linear time algorithm for computing exact euclidean distance transforms of binary images in arbitrary dimensions," *IEEE Transactions on Pattern Analysis and Machine Intelligence*, vol. 25, no. 2, pp. 265–270, 2003.

[11] Cárdenes, R., Pozo, J., Bogunovic, H., Larrabide, I., and Frangi, A., "Automatic aneurysm neck detection using surface voronoi diagrams," *IEEE Transactions on Medical Imaging*, vol. 30, no. 10, pp. 1863–1876, 2011.

[12] CARMA. `http://insight-journal.org/midas/collection/view/197`.

[13] Caselles, V., Kimmel, R., and Sapiro, G., "Geodesic active contours," *International Journal of Computer Vision*, vol. 22, no. 1, pp. 61–79, 1997.

[14] Chan, T. and Vese, L., "Active contours without edges," *IEEE Transactions on Image Processing*, vol. 10, no. 2, pp. 2029–2039, 2001.

[15] Cheng, L., Burchard, P., Merriman, B., and Osher, S., "Motion of curves constrained on surfaces using a level set approach," *Journal of Computational Physics*, vol. 175, pp. 604–644, 2002.

[16] Cootes, T., Edwards, G., and Taylor, C., "Active appearance models," *IEEE Transactions on Pattern Analysis and Machine Intelligence*, vol. 23, pp. 681–685, June 2001.

[17] Cootes, T., Taylor, C., Cooper, D., and Graham, J., "Active shape models-their training and application," *Computer Vision and Image Understanding*, vol. 61, no. 1, pp. 38–59, 1995.

[18] Crick, S., Sheppard, M., Ho, S., Gebstein, L., and Anderson, R., "Anatomy of the pig heart: comparisons with normal human cardiac structure," *Journal of Anatomy*, vol. 193, pp. 105–119, 1998.

[19] Crum, W. R., Camara, O., and Hill, D. L., "Generalized overlap measures for evaluation and validation in medical image analysis," *IEEE Transaction on Medical Imaging*, vol. 25, no. 11, pp. 1451–1461, 2006.

[20] Danielsson, P., "Euclidean distance mapping," *Computer Graphics and Image Processing*, vol. 14, pp. 227–248, 1980.

[21] Dempster, A. P., Laird, N. M., and Rubin, D. B., "Maximum likelihood from incomplete data via the em algorithm," *JOURNAL OF THE ROYAL STATISTICAL SOCIETY, SERIES B*, vol. 39, no. 1, pp. 1–38, 1977.

[22] Depa, M., Sabuncu, M., Holmvang, G., Nezafat, R., Schmidt, E., and Golland, P., "Robust atlas-based segmentation of highly variable anatomy: Left atrium segmentation," in *In Proceedings of MICCAI Workshop on Statistical Atlases and Computational Models of the Heart: Mapping Structure and Function*, vol. 6364 of *Lecture Notes in Computer Science*, pp. 85–94, 2010.

[23] Desbrun, M., Meyer, M., Schröder, P., and Barr, A. H., "Implicit fairing of irregular meshes using diffusion and curvature flow," in *SIGGRAPH*, pp. 317–324, 1999.

[24] Dijkstra, E., "A note on two problems in connexion with graphs," *Numerische Mathematik*, vol. 1, pp. 269 – 271, 1959.

[25] Ecabert, O., Peters, J., Schramm, H., Lorenz, C., von Berg, J., Walker, M., Vembar, M., Olszewski, M. E., Subramanyan, K., Lavi, G., and Weese, J., "Automatic model-based segmentation of the heart in ct images," *IEEE Transaction on Medical Imaging*, vol. 27, no. 9, pp. 1189–1201, 2008.

[26] Essafi, S., Langs, G., and Paragios, N., "Hierarchical 3d diffusion wavelet shape priors," in *International Conference on Computer Vision*, pp. 1717–1724, 2009.

[27] Faber, T., Santana, C., Garcia, E., Candell-Riera, J., Folks, R., Peifer, J., Hopper, A., Aguade, S., Angel, J., and Klein, J., "Three-dimensional fusion of coronary arteries with myocardial perfusion distributions: clinical validation," *Journal of Nuclear Medicine*, vol. 45, no. 5, pp. 745–753, 2004.

[28] Foulonneau, A., Charbonnier, P., and Heitz, F., "Affine-invariant geometric shape priors for region-based active contours," *IEEE Transactions on Pattern Analysis and Machine Intelligence*, vol. 28, no. 8, pp. 1352–1357, 2006.

[29] Frakes, W. and Baeza-Yates, R., eds., *Information Retrieval: Data Structures & Algorithms*. Prentice-Hall, 1992.

[30] Fritz, D., Unterhinninghofen, R., Dillmann, R., Rinck, D., and Scheuering, M., "Automatic segmentation of the left ventricle and computation of diagnostic parameters using regiongrowing and a statistical model," in *Proceedings of SPIE Medical Imaging*, vol. 5747, pp. 1844–1854, 2005.

[31] Gao, Y., Gholami, B., MacLeod, R., Blauer, J., Haddad, W., and Tannenbaum, A., "Segmentation of the endocardial wall of the left atrium using local region-based active contours and statistical shape learning," in *Proceedings of SPIE Medical Imaging*, 2010.

[32] Gao, Y. and Tannenbaum, A., "Combining atlas and active contour for automatic 3d medical image segmentation," in *International Symposium on Biomedical Imaging*, pp. 1401–1404, 2011.

[33] Gao, Y., Tannenbaum, A., and Kikinis, R., "Simultaneous multi-object segmentation using local robust statistics and contour interaction," in *MICCAI Workshop on Medical Computer Vision*, 2010.

[34] Insight Segmentation and Registration Toolkit (ITK). `http://www.itk.org/`.

[35] ISBI Challenges 2012: cDEMRIS. `http://www.biomedicalimaging.org/2012/index.php/programme/isbi-challenges/1`.

[36] Ishihara, Y., Nazafat, R., Wylie, J., Linguraru, M., Josephson, M., Howe, R., Manning, W., and Peters, D., "MRI evaluation of rf ablation scarring for atrial fibrillation treatment," in *Proceedings of SPIE Medical Imaging*, vol. 6590, 2007.

[37] Jaïs, P., Weerasooriya, R., Shah, D., Hocini, M., Macle, L., Choi, K., Scavee, C., Haïssaguerre, M., and Clémenty, J., "Ablation therapy for atrial fibrillation (AF)," *Cardiovascular research*, vol. 54, no. 2, pp. 337–346, 2002.

[38] John, M. and Rahn, N., "Automatic left atrium segmentation by cutting the blood pool at narrowings," in *MICCAI (2)*, pp. 798–805, 2005.

[39] John, M. and Rahn, N., "Automatic left atrium segmentation by cutting the blood pool at narrowings," in *Proceedings of the 8th international conference on Medical image computing and computer-assisted intervention - Volume Part II*, MICCAI'05, pp. 798–805, 2005.

[40] Jolly, M., "Automatic segmentation of the left ventricle in cardiac mr and ct images," *International Journal of Computer Vision*, vol. 70, no. 2, pp. 151–163, 2006.

[41] Kaplansky, L. and Tal, A., "Mesh segmentation refinement," *Pacific Graphics*, vol. 28, no. 7, pp. 1995–2003, 2009.

[42] Karim, R., Mohiaddin, R., and Rueckert, D., "Left atrium segmentation for atrial fibrillation ablation," in *Proceedings of SPIE Medical Imaging*, 2008.

[43] Karim, R., Arujuna, A., Brazier, A., Gill, J. S., Rinaldi, C. A., O'Neill, M., Razavi, R., Schaeffter, T., Rueckert, D., and Rhode, K. S., "Automatic segmentation of left atrial scar from delayed-enhancement magnetic resonance imaging," in *the Sixth International Conference on Functional Imaging and Modeling of the Heart(FIMH)*, pp. 63–70, 2011.

[44] Kass, M., Witkin, A., and Terzopoulos, D., "Snakes: Active contour models," *International journal of computer vision*, vol. 1, no. 4, pp. 321–331, 1998.

[45] Katz, S., Leifman, G., and Tal, A., "Mesh segmentation using feature point and core extraction," *The Visual Computer*, vol. 21, no. 8-10, pp. 649–658, 2005.

[46] Katz, S. and Tal, A., "Hierarchical mesh decomposition using fuzzy clustering and cuts," *ACM Transactions on Graphics*, vol. 22, pp. 954–961, July 2003.

[47] Khotanzad, A. and Hong, Y. H., "Invariant image recognition by zernike moments," *IEEE Transaction on Pattern Analysis and Machine Intelligence*, vol. 12, no. 5, pp. 489–497, 1990.

[48] Kichenassamy, S., Kumar, A., Olver, P., Tannenbaum, A., and Yezzi, A., "Gradient flows and geometric active contour models," in *Proceedings of the Fifth International Conference on Computer Vision*, ICCV '95, (Washington, DC, USA), pp. 810–815, IEEE Computer Society, 1995.

[49] Kimmel, R. and Sethian, J., "Computing geodesic paths on manifolds," in *Proceedings of the National Academy of Sciences of the United States of America*, pp. 8431–8435, 1998.

[50] Lai, R. and Chan, T., "A framework for intrinsic image processing on surfaces," *Computer Vision and Image Understanding*, vol. 115, no. 12, pp. 1647–1661, 2011.

[51] Lankton, S., Nain, D., Yezzi, A., and Tannenbaum, A., "Hybrid geodesic region-based curve evolutions for image segmentation," in *Proceedings of SPIE Medical Imaging*, 2007.

[52] Lankton, S. and Tannenbaum, A., "Localizing region-based active contours," *IEEE Transactions on Image Processing*, pp. 2029–2039, 2008.

[53] Le, H., Wong, J. T., and Molloi, S., "Estimation of regional myocardial mass at risk based on distal arterial lumen volume and length using 3d micro-ct images,"

[54] Lempitsky, V., Verhoek, M., Noble, J. A., and Blake, A., "Random forest classification for automatic delineation of myocardium in real-time 3d echocardiography," in *the Fifth International Conference on Functional Imaging and Modeling of the Heart*, pp. 447–456, 2009.

[55] Leventon, M. E., Grimson, W. E. L., and Faugeras, O. D., "Statistical shape influence in geodesic active contours," in *CVPR*, pp. 1316–1323, 2000.

[56] Lorensen, W. and Cline, H., "Marching cubes: A high resolution 3d surface construction algorithm," *SIGGRAPH Computer Graphics*, vol. 21, pp. 163–169, August 1987.

[57] Lynch, M., Ghita, O., and Whelan, P., "Automatic segmentation of the left ventricle cavity and myocardium in mri data," *Computers in Biology and Medicine*, vol. 36, pp. 389–407, Apr. 2006.

[58] Lynch, M., Ghita, O., and Whelan, P., "Left-ventricle myocardium segmentation using a coupled level-set with a priori knowledge," *Computerized Medical Imaging and Graphics*, vol. 30, no. 4, pp. 255–262, 2006.

[59] Mattes, D., Haynor, D. R., Vesselle, H., Lewellen, T. K., and Eubank, W., "Pet-ct image registration in the chest using free-form deformations," *IEEE Transaction on Medical Imaging*, vol. 22, no. 1, pp. 120–128, 2003.

[60] McGann, C., Kholmovski, E., Oakes, R., Blauer, J., Daccarett, M., Segerson, N., Airey, K., Akoum, N., Fish, E., Badger, T., DiBella, E., Parker, D., MacLeod, R., and Marrouche, N., "New magnetic resonance imaging based method to define extent of left atrial wall injury after the ablation of atrial fibrillation," *Journal of the American College of Cardiology*, 2008.

[61] Mitchell, S., Lelieveldt, B., van der Geest, R., Bosch, J., Reiber, J. C., and Sonka, M., "Multistage hybrid active appearance model matching: Segmentation of left and right ventricles in cardiac mr images," *IEEE Transactions on Medical Imaging*, vol. 20, no. 5, pp. 415–423, 2001.

[62] Novotni, M. and Klein, R., "3d zernike descriptors for content based shape retrieval," in *Symposium on Solid Modeling and Applications*, pp. 216–225, 2003.

[63] Osher, S. and Sethian, J., "Fronts propagating with curvature dependent speed: Algorithms based on hamilton-jacobi formulation," *Journal of Computational Physics*, vol. 79, pp. 12–49, 1988.

[64] Otsu, N., "A threshold selection method from gray-level histograms," *IEEE Transactions on Systems, Man, and Cybernetics*, vol. 9, no. 1, pp. 62–66, 1979.

[65] Paragios, N., "A level set approach for shape-driven segmentation and tracking of the left ventricle," *IEEE Transactions on Pattern Analysis and Machine Intelligence*, vol. 22, no. 6, pp. 776–773, 2003.

[66] Perry, D., Morris, A., Burgon, N., McGann, C., MacLeod, R., and Cates, J., "Automatic classication of scar tissue in late gadolinium enhancement cardiac MRI for the assessment of left-atrial wall injury after radiofrequency ablation," in *Proceedings of SPIE Medical Imaging:Computer Aided Diagnosis*, 2012.

[67] Petitjean, C. and Dacher, J., "A review of segmentation methods in short axis cardiac mr images," *Medical Image Analysis*, vol. 15, no. 2, pp. 169–184, 2011.

[68] Rose, J.-L., Revol-Muller, C., Charpigny, D., and Odet, C., "Shape prior criterion based on tchebichef moments in variational region growing," in *International Conference on Image Processing (ICIP)*, pp. 1081–1084, 2009.

[69] Rose, J.-L., Revol-Muller, C., Langlois, J.-B., Janier, M., and Odet, C., "3d region growing integrating adaptive shape prior," in *ISBI*, pp. 967–970, 2008.

[70] Rueckert, D., Sonoda, L., Hayes, C., Hill, D., Leach, M., and Hawkes, D., "Nonrigid registration using free-form deformations: Application to breast mr images," *IEEE Transactions on Medical Imaging*, vol. 18, pp. 712–721, 1999.

[71] Seiler, C., Kirkeeide, R., and Gould, K., "Measurement from arteriograms of regional myocardial bed size distal to any point in the coronary vascular tree for assessing anatomic area at risk," *Journal of the American College of Cardiology*, vol. 21, no. 3, pp. 783–797, 1993.

[72] Sethian, J., "A fast marching level set method for monotonically advancing fronts," in *Proceedings of the National Academy of Sciences of the United States of America*, pp. 1591–1595, 1995.

[73] Shamir, A., "A survey on mesh segmentation techniques," *Computer Graphics Forum*, vol. 27, no. 6, pp. 1539–1556, 2008.

[74] Sundaramoorthi, G., Yezzi, A., and Mennucci, A., "Sobolev active contours," *International Journal of Computer Vision*, vol. 73, no. 3, pp. 345–366, 2007.

[75] Surazhsky, V., Surazhsky, T., Kirsanov, D., Gortler, S. J., and Hoppe, H., "Fast exact and approximate geodesics on meshes," *ACM Transaction Graphics*, vol. 24, pp. 553–560, July 2005.

[76] Suri, J., "Computer vision, pattern recognition and image processing in left ventricle segmentation: The last 50 years," *Pattern Analysis and Applications*, vol. 3, no. 3, pp. 209–242, 2000.

[77] The World Health Report World Health Organization (WHO). `http://www.who.int/`, 2003.

[78] Tsai, A., Yezzi, A., III, W. W., Tempany, C., Tucker, D., Fan, A., Eric, W., Grimson, L., and Willsky, A., "A shape-based approach to the segmentation of medical imagery using level sets," *IEEE Transactions on Medical Imaging*, vol. 22, no. 2, pp. 137–154, 2003.

[79] van Rikxoort, E., Isgum, I., Arzhaeva, Y., Staring, M., Klein, S., Viergever, M., Pluim, J., and van Ginneken, B., "Adaptive Local Multi-Atlas Segmentation: Application to the Heart and the Caudate Nucleus," *Medical Image Analysis*, vol. 14, no. 1, pp. 39–49, 2010.

[80] Viola, P. and Viola, P. A., "Alignment by maximization of mutual information," in *International Journal of Computer Vision*, pp. 16–23, 1995.

[81] Visualization Toolkit (VTK). `http://www.vtk.org/`.

[82] Whitaker, R., "A level-set approach to 3d reconstruction from range data," *International Journal of Computer Vision*, vol. 29, pp. 203–231, Sept. 1998.

[83] Xu, S.-G., Zhang, Y.-X., and Yong, J.-H., "A fast sweeping method for computing geodesics on triangular manifolds," *IEEE Transactions on Pattern Analysis and Machine Intelligence*, vol. 32, no. 2, pp. 231–241, 2010.

[84] Y. Gao, L. Zhu, A. Y. S. B. and Tannenbaum, A., "Delayed-enhancement MRI segmentation using distance and intensity criteria," in *IEEE International Symposium on Biomedical Imaging(ISBI)*, 2012.

[85] Zeng, X., Staib, L., Schultz, R., and Duncan, J., "Segmentation and measurement of the cortex from 3d MR images using coupled surfaces propagation," *IEEE Transactions on Medical Imaging*, vol. 18, no. 10, pp. 927–937, 1999.

[86] Zhang, C. and Chen, T., "Efficient feature extraction for 2d/3d objects in mesh representation," in *International Conference on Image Processing (ICIP) (3)*, pp. 935–938, 2001.

[87] Zhao, H., Chan, T., Merriman, B., and Osher, S., "A variational level set approach to multiphase motion," *Journal of Computational Physics*, vol. 127, no. 1, pp. 179–195, 1996.

[88] Zhao, H., "A fast sweeping method for eikonal equations.," *Mathematics of Computation*, vol. 74, no. 250, pp. 603–627, 2005.

[89] Zheng, Y., Barbu, A., Georgescu, B., Scheuering, M., and Comaniciu, D., "Four-chamber heart modeling and automatic segmentation for 3-D cardiac ct volumes using marginal space learning and steerable features," *IEEE Transactions on Medical Imaging*, vol. 27, no. 11, pp. 1668–1681, 2008.

[90] Zheng, Y., Wang, T., John, M., Zhou, S. K., Boese, J. M., and Comaniciu, D., "Multi-part left atrium modeling and segmentation in c-arm ct volumes for atrial fibrillation ablation," in *MICCAI (3)*, pp. 487–495, 2011.

[91] Zhu, L., Gao, Y., Yezzi, A., Arepalli, C., Faber, T., Stillman, A., and Tannenbaum, A., "Automatic segmentation of left ventricular myocardium from ct images using shape decomposition and contour evolution," *IEEE Transactions on Image Processing*, (submitted).

[92] Zhu, L., Gao, Y., Yezzi, A., Faber, T., Stillman, A., and Tannenbaum, A., "Automatic segmentation of left ventricular myocardium from ct images using shape decomposition and contour evolution," *IEEE Transactions on Medical Imaging*, (submitted).

[93] Zhu, L., Mohan, V., Stillman, A., Faber, T., and Tannenbaum, A., "Estimation of myocardial volume at risk from ct angiography," in *Proceedings of SPIE Medical Imaging*, pp. 79632A–79632A6, 2011.

[94] Zhu, S. C. and Yuille, A., "Region competition: Unifying snakes, region growing, and bayes/mdl for multi-band image segmentation," *IEEE Transactions on Pattern Analysis and Machine Intelligence*, vol. 18, pp. 884–900, 1996.

[95] Zhuang, X., Rhode, K., Razavi, R., Hawkes, D., and Ourselin, S., "A registration-based propagation framework for automatic whole heart segmentation of cardiac MRI," *IEEE Transaction on Medical Imaging*, vol. 29, no. 9, pp. 1612–1625, 2010.

[96] Zimmer, C. and Olivo-Marin, J., "Coupled parametric active contours," *IEEE Transactions on Pattern Analysis and Machine Intelligence*, vol. 27, no. 11, pp. 1838–1842, 2005.

[97] Zucker, S. W., "Region growing: Childhood and adolescence," *Computer Graphics and Image Processing*, vol. 5, pp. 382–399, Sept. 1976.

VITA

Liangjia Zhu was born in Baojing, Hunan Province in China on May 23rd, 1979. He received a Master of Science in Control Theory and Application in 2003 from National University of Defense Technology, Changsha, China. After working several years in universities and companies, he started his doctorate research at Georgia Institute of Technology in 2010. He has been a graduate research assistant in the Minerva research lab since 2010 and his doctorate research has focused on computer vision and medical image analysis.